Ultrasonics Sonochemistry 83 (2022) 105925

Contents lists available at ScienceDirect

Ultrasonics Sonochemistry

journal homepage: www.elsevier.com/locate/ultson

The importance of chemical mechanisms in sonochemical modelling

Csanád Kalmár [a,*], Tamás Turányi [b], István Gy. Zsély [b], Máté Papp [b], Ferenc Hegedűs [a]

[a] Department of Hydrodynamic Systems, Faculty of Mechanical Engineering, Budapest University of Technology and Economics, Műegyetem rkp. 3., H-1111 Budapest, Hungary

[b] Chemical Kinetics Laboratory, Institute of Chemistry, ELTE Eötvös Loránd University, Budapest, Hungary

ARTICLE INFO

Keywords:
Bubble dynamics
Sonochemistry
Chemical modeling
Chemical reactions
Reaction mechanisms

ABSTRACT

A state-of-the-art chemical mechanism is introduced to properly describe chemical processes inside a harmonically excited spherical bubble placed in water and saturated with oxygen. The model uses up-to-date Arrhenius-constants, collision efficiency factors and takes into account the pressure-dependency of the reactions. Duplicated reactions are also applied, and the backward reactions rates are calculated via suitable thermodynamic equilibrium conditions. Our proposed reaction mechanism is compared to three other chemical models that are widely applied in sonochemistry and lack most of the aforementioned modelling issues. In the governing equations, only the reaction mechanisms are compared, all other parts of the models are identical. The chemical yields obtained by the different modelling techniques are taken at the maximum expansion of the bubble. A brief parameter study is made with different pressure amplitudes and driving frequencies at two equilibrium bubble sizes. The results show that due to the deficiencies of the former reaction mechanisms employed in the sonochemical literature, several orders of magnitude differences of the chemical yields can be observed. In addition, the trends along a control parameter can also have dissimilar characteristics that might lead to false optimal operating conditions. Consequently, an up-to-date and accurate chemical model is crucial to make qualitatively and quantitatively correct conclusions in sonochemistry.

1. Introduction

In sonochemical reactors, a liquid domain is irradiated with high-intensity, high-frequency acoustic field in the ultrasound regime [1]. As a result, the dissolved gas content in the liquid—mixed with water vapour—tends to form numerous bubbles [2,3] which assemble into clouds, often called bubble clusters [4,5]. Due to the oscillating pressure field, these bubbles pulsate around their equilibrium size demonstrated by various experiments in the last couple of decades [6–9].

If the acoustic amplitude, expressed in pressure, is sufficiently high (practically exceeding the ambient pressure), the bubble radius can grow up to even 20–30 times its equilibrium value in the expansion phase [10]. Due to the large inertia of the liquid, the bubbles undergo extremely rapid compression in the positive pressure change phase (depending on the employed frequency). This phenomenon is usually called *bubble collapse*. The resulting final peak internal temperature and pressure can reach several thousands of kelvins and hundreds of bars, respectively [11–13].

Under these extreme circumstances, chemical reactions can take place, i.e., dissociation of water, oxygen or even nitrogen molecules [14,15]. Evidently, the produced species like atomic O or H, H_2O_2 and many other molecules tend to react further with each other, resulting in a complex interaction between all the species. These complex chemical reactions are used in several applications, like in wastewater-treatment [16,17], pharmaceutical industry [18] or even synthesizing nanocrytals [19,20] and other chemical substances [21,22]. The physical effects of acoustic cavitation is also utilized in medicine, for example in sonodynamic therapy [23–25].

The radial dynamics (periodic or chaotic oscillations) of a single bubble (excluding chemistry) has become fairly well-known in the last decades [26–28]. Several investigations [29–31] have discovered the effect of the excitation parameters, bubble size, and even the effects of dual-frequency driving [32–34]. Different metrics for the collapse strength (e.g., compression ratio) were often introduced to characterize the cavitation/chemical activity of a bubble by simple means [35–39].

Another direction of sonochemical research is the quantitative modelling of the chemical processes inside bubbles [40–42]. This is a significantly more difficult approach: the rates of all the chemical

* Corresponding author.
E-mail addresses: cskalmar@hds.bme.hu (C. Kalmár), turanyi@chem.elte.hu (T. Turányi), zsigy@chem.elte.hu (I.Gy. Zsély), papp.matyi66@gmail.com (M. Papp), hegedusf@hds.bme.hu (F. Hegedűs).

https://doi.org/10.1016/j.ultsonch.2022.105925
Received 22 November 2021; Received in revised form 11 January 2022; Accepted 16 January 2022
Available online 22 January 2022

reactions have to be precisely calculated. The size of the kinetic differential equation system grows drastically, as well as its complexity [43]. For example, Storey and Szeri [44] was among the firsts who introduced chemical modelling in bubbles. They solved the complete reaction–diffusion system of partial differential equations of an *n*-component system. However, the kinetic model was limited to a couple of parameter combinations only, presumably due to the model complexity and the limited available computing power. Even after two decades since the investigation of Storey and Szeri, the majority of the studies still employ the spatially homogeneous bubble approach (including the present paper); that is, the interior concentrations are homogeneous that reduces the governing equations into a moderately large ordinary differential equation system. In the next couple of paragraphs, the main contributions of different research groups to the better understanding of the behaviour of a chemically active bubble are summarised briefly.

From the early 1990s, chemical calculations started to be published continuously. Besides the excellent work of Storey and Szeri mentioned above, Yasui and his co-workers published numerous exceptional works from 1995. He established a proper evaporation–condensation approach [45] as well as a linear heat conduction approximation [46]. He made several calculations with pure O_2 [47] and air bubbles [48]. He found optimal bubble temperatures in air bubbles in terms of different oxidant production, like OH radical, O atom or H_2O_2 molecule [49]. He also examined the effect of several ambient parameters, for example, ambient radius, temperature or pressure [50,51].

In 1993, Kamath et al. [52] reported a theoretical approach of chemical calculations based on the hydrogen combustion chemical kinetic model of Egolfopoulos and Law [53]. They used the detailed temperature-distribution model of Prosperetti [54] for precise temperature estimation. Based on the work of Kamath, Lohse and his group released various outstanding studies about sonochemical processes: they introduced a convenient method for heat conduction estimation [55,56], they constructed detailed phase-diagrams for various gas compositions [57], and they also examined radical production as a function of driving frequency and pressure amplitude [58].

From the mid-2000s, Hamdaoui, Merouani, Kerboua and their group have also published studies regularly about chemically active single bubble [59–61]. Only to name a few from their extensive work: they examined the sensitivity of free radicals on different gas content [62], studied the effect of multiple driving frequencies [63], or even made energy-efficiency considerations [64].

Presumably, the reason of the biggest challenge in sonochemical modelling is that the rates of most chemical reactions have *exponential* dependence on the temperature. This fact results in an extreme sensitivity on the model parameters and demands a precise and up-to-date validation process (e.g. for the Arrhenius constants). Most of the applied chemical mechanisms in the works mentioned above tend to lack an advanced validation method, and their model parameters are often outdated. For example, Storey and Szeri use a mechanism from 1988 [65]; Yasui in [48] adopts his mechanism from the 1980s [66], or Merouani et al. in [67] referred to studies from 2004 and 1999. The reaction equations and their parameters are often taken from previous studies, sometimes resulting in chain-references to decades old models. *The primary goal of the present study is to break this habit and to use a state-of-the-art reaction mechanism, and compare the chemical output of a bubble by employing our and the most important reaction mechanisms available in the relevant sonochemical literature.*

Besides using up-to-date parameters in the reaction mechanism, there are other modelling issues which are usually neglected during the computation of a chemically active bubble. For example, the so-called three-body reactions are occasionally taken into account, but *enhanced* third-body efficiencies for specific molecules are rarely specified. In addition, pressure-dependence of reaction rates is seldom included in the mechanisms, although it can change the chemical rates significantly due to the high compression ratio inside a bubble. Finally, the rate constants of some specific reactions can have a more complex dependence on the temperature than exponential; this needs a special care. The reader is referred to Sec. 2.2 for a detailed description.

In the present paper, *a precisely validated, up-to-date chemical mechanism* for a single, sonochemically active bubble is introduced, which takes into account all the aforementioned modelling issues. As a test case, the reaction mechanism is built-up for a bubble that initially contains pure oxygen and water vapour. Nevertheless, Sec. 2.2 can also be regarded as a "guideline" how to build-up a proper, state-of-the-art reaction mechanism for other bubble compositions (e.g., air bubble). Naturally, the modelling constants have to be always taken form the latest corresponding publications or databases. The NIST Chemical Kinetics Database [68] is the traditional, very comprehensive database of rate parameters, but it is nowadays not updated systematically. The *k-evaluation* web page [69] contains a continuously updated list of rate parameters of elementary reactions of several high temperature reaction systems, including the hydrogen–oxygen system. The listed rate parameters were directly measured, theoretically calculated based on first principles, fitted to indirect experimental data or used in previous modelling studies.

The performance of our proposed modelling technique in terms of chemical yield is compared with three other reaction mechanisms, which are extensively employed in sonochemistry by other research groups (Yasui; Kamath and Lohse; Hamdaoui, Merouani and Kerboua). The basis of the comparison is the replacement of the reaction mechanism *only*. The rest of the governing equations are identical to clearly identify the effect of chemical kinetics. The major differences between the reaction mechanisms are discussed in Sec. 2.4.

Numerical simulations are made with different driving parameters (pressure amplitude and frequency) at two different bubble sizes. Results show that employing an outdated reaction mechanism can lead to orders of magnitude differences in the chemical yield. In addition, even the trends of the yield as a function of a control parameter might have different characteristics leading to false optimal operating conditions. Therefore, employing an up-to-date and accurate reaction mechanism introduced in this study is crucial to make qualitatively and quantitatively correct conclusions in sonochemistry. For reproducibility reasons, all the employed numerical codes are available as Supplementary material.

2. Governing equations

The mathematical model of a sonochemical bubble can be separated into two main parts: physical and chemical. The physical part of the model describes the temporal evolution of the bubble radius, temperature and pressure, while the chemical part focuses on the chemical processes and the rates of the chemical reactions. This approach is convenient for the comparison of different chemical reaction mechanisms. That is, the physical part of the model can be kept fixed, and only the reaction mechanism needs to be replaced. Thus, the difference between the chemical mechanisms can be examined precisely.

Keep in mind that the papers cited in Sec. 1 have a variety of slightly different approaches in the physical modelling. For instance, the approximation of the heat loss across the bubble wall, the computation of the material properties of the chemical components inside the bubble or the employed equation of state of the gas composition (e.g., ideal gas or Van der Waals). In order to clearly separate the effect of the chemical kinetics, only the reaction mechanisms are adopted from these papers.

Although the present paper focuses only on the influence of the reaction mechanisms, a sufficiently complex physical model is employed for the proper estimation of the peak temperature and temperature loss, the evaporation/condensation of water vapour and the computation of the material properties of the gas mixture. These quantities are critical for chemical processes. For the modelling details, see Sec. 2.1.

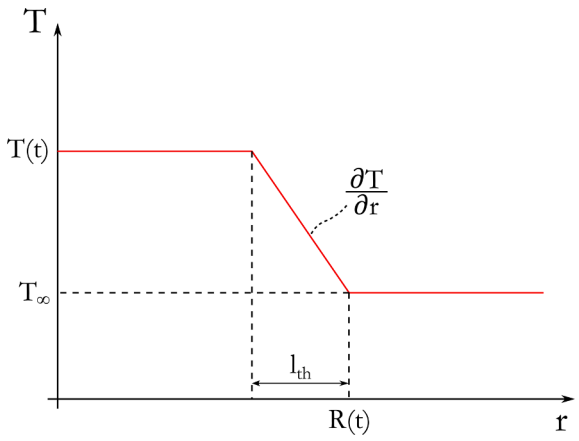

Fig. 1. The simplified temperature distribution. The temperature changes linearly from T to T_∞ in the thermal boundary layer.

2.1. The physical model

The following general assumptions are applied during the physical modelling. The bubble is separated and considered spherically symmetric. The liquid is water subjected to harmonic pressure excitation. The bubble interior initially contains non-condensable gas (oxygen) and water vapour. Due to the chemical reactions, the composition of the bubble interior continuously varies. This gas content inside the bubble is considered as an ideal mixture of ideal gases. The pressure, temperature and the concentrations of the components inside the bubble are spatially uniform except in a thin thermal boundary layer. Heat transfer via a boundary layer approximation, and non-equilibrium evaporation and condensation of water vapour are involved in the model. The diffusion of the chemical species (other than water vapour) into the liquid domain is neglected assuming that the time scale of the diffusion is much larger then the oscillation period of the bubble (the length of the simulations are only few acoustic cycles).

The inertia of the liquid domain has the most important effect on the radial dynamics of a bubble. This is the main reason for the developed high compression ratio during the collapse phase: to stop the liquid moving towards the center of the bubble, a high internal pressure has to build-up (even hundreds of atmospheres [1]). Due to such an extreme dynamics, the liquid compressibility has to be taken into account. The modified Keller–Miksis equation [70] (and its various forms) is a widely used equation in sonochemistry to model the inertial effect (valid approximately up to Mach number 0.3 [71]). It is given as

$$\left(1-\frac{\dot{R}}{c_L}\right)R\ddot{R}+\left(1-\frac{\dot{R}}{3c_L}\right)\frac{3}{2}\dot{R}^2=\left(1+\frac{\dot{R}}{c_L}+\frac{R}{c_L}\frac{d}{dt}\right)\frac{(p_L-p_\infty(t))}{\rho_L}, \tag{1}$$

where $R(t)$ is the radius of the bubble, t is the time, c_L is the sound speed in the liquid and ρ_L is the density of the liquid. p_L is the liquid pressure at the bubble wall which is related to the internal pressure (p) via the boundary condition

$$p=p_L+\frac{2\sigma}{R}+4\mu_L\frac{\dot{R}}{R}. \tag{2}$$

Here, σ is the surface tension and μ_L is the dynamic viscosity of the liquid. The dots stand for derivatives with respect to time. The far field pressure p_∞ contains the harmonic ultrasound excitation as

$$p_\infty(t)=P_\infty+p_A\sin(2\pi ft), \tag{3}$$

where P_∞ is the ambient pressure, p_A and f are the ultrasound pressure amplitude and frequency, respectively.

In order to calculate p in Eq. (2), an equation of state has to be applied. Here, we assume ideal gas for the mixture indicating

$$p=MR_gT, \tag{4}$$

where M is the total concentration of the mixture, R_g is the universal gas constant and T is the temperature. The concentration of each component is described later in details (see Sec. 2.2).

The temperature is calculated by solving the first law of thermodynamics in the time-dependent form of

$$\dot{T}=\frac{-p\dot{V}+\sum\dot{Q}}{n_t\overline{C}_v}, \tag{5}$$

where $V=4R^3\pi/3$ is the volume of the bubble, $\sum\dot{Q}$ is the sum of heat diffusion and reaction heats (their exact formulae are presented later). n_t is the total amount of substance of the mixture in moles and $\overline{C}_v$ is the average molar heat capacity of the mixture at constant volume.

Various thermodynamic quantities (heat capacities, enthalpies, entropies) are calculated using the NASA chemical equilibrium code [72]. This assumes that these properties are the functions of temperature only and they are given in terms of polynomial fits as

$$\frac{C_{p,k}}{R_g}=\sum_{n=1}^{N}a_{n,k}T^{n-1}, \tag{6}$$

$$\frac{H_k}{R_gT}=\sum_{n=1}^{N}\frac{a_{n,k}T^{n-1}}{n}+\frac{a_{N+1,k}}{T}, \tag{7}$$

$$\frac{S_k}{R_g}=a_{1,k}\ln T+\sum_{n=2}^{N}\frac{a_{n,k}T^{n-1}}{n-1}+a_{N+2,k}. \tag{8}$$

Here, $k=1\ldots K$ is the index of the chemical components, where $K=10$ is the total number of the components in the mixture. $C_{p,k}$ stands for molar heat capacity at constant pressure, H_k is the enthalpy of formation and S_k is the entropy of component k. For the NASA polynomials, $a_{n,k}$ are the polynomial coefficients for component k and $N=5$. It is worth noting that NASA polynomials have different sets of $a_{n,k}$ coefficients for intervals $[T_{\text{low}},T_{\text{mid}}]$ and $[T_{\text{mid}},T_{\text{high}}]$. If $T<T_{\text{low}}$ or $T>T_{\text{high}}$, the values for the low or high bound are used, respectively. Consequently, $(N+2)\cdot 2=14$ coefficients belong to each chemical component. T_{low}, T_{mid} and T_{high} can also be different for each component. The applied values of $a_{n,k}$ and other parameters are shown in Tables A.6 and A.5.

The molar heat capacities at constant volume are calculated as

$$C_{v,k}=C_{p,k}-R_g. \tag{9}$$

Some average values of the mixture are calculated as follows. The mole fraction of component k is defined as

$$X_k=\frac{c_k}{M}, \tag{10}$$

where c_k is the molar concentration of component k, and the total concentration M is the sum of each concentration ($M=\sum c_k$). Most average values of the mixture are the weighted average of the components with respect to the mole fractions, such as

$$\overline{W}=\sum_{k=1}^{K}X_kW_k, \tag{11}$$

$$\overline{\rho}=\sum_{k=1}^{K}c_kW_k, \tag{12}$$

$$\overline{C}_p=\sum_{k=1}^{K}X_kC_{p,k}, \tag{13}$$

$$\overline{C}_v=\sum_{k=1}^{K}X_kC_{v,k}, \tag{14}$$

where W is the molecular weight, ρ is the density, and the overline means averaged values for the mixture. It is worth emphasizing again that the equations above are only valid for the assumption of ideal gases.

Heat conduction between the fluid and the bubble interior is modelled with the approach used by several authors in the past [55,73]. Zhou and Prosperetti made an excellent work on thermal modeling recently [74], the interested reader is referred to their paper. In their conclusion, in the case of violent collapses, introducing a thermal boundary layer is an appropriate method for precisely modeling heat fluxes. In this boundary layer, the temperature changes linearly from the bubble mean temperature T to the ambient liquid temperature T_∞, which is kept constant. A sketch about the simplified temperature distribution is shown in Fig. 1. In this approach, the amount of heat transfer is approximated as

$$\dot{Q}_{th} = A\bar{\lambda}\frac{\partial T}{\partial r}\Big|_{r=R} \approx A\bar{\lambda}\,\frac{T_\infty - T}{l_{\text{th}}}, \tag{15}$$

where A is the area of the bubble surface, $\bar{\lambda}$ is the averaged thermal conductivity of the mixture and l_{th} is the thickness of the thermal boundary layer calculated as

$$l_{\text{th}} = \min\left(\sqrt{\frac{\bar{\chi}}{\dot{R}}}, \frac{R}{\pi}\right), \tag{16}$$

where $\bar{\chi}$ is the averaged thermal diffusivity of the mixture. $\bar{\lambda}$ is calculated similarly as the other averaged values; that is,

$$\bar{\lambda} = \sum_{k=1}^{K} X_k \lambda_k\,, \tag{17}$$

where the λ_k values are collected in Table A.5. Using $\bar{\lambda}$, the average thermal diffusivity is

$$\bar{\chi} = \frac{\bar{\lambda}}{\bar{c}_p\bar{\rho}} = \frac{\bar{\lambda}}{\frac{\bar{c}_p}{\bar{W}}\bar{\rho}}\,. \tag{18}$$

Note that some λ_k values are not indicated, because their exact values were not found in the literature; these are excluded from the averaging process in Eq. (17). Since the gas mixture contains dominantly oxygen and water vapour (as it is shown in later sections), this neglection does not have significant effect.

Heat diffusion is a rather important phenomenon that damps temperature peaks during violent collapses. Since temperature is one of the most influential variables regarding the chemical processes, a proper estimation of heat transfer is essential. The other part of heat source is the reaction heat that is defined later in Sec. 2.2.

The evaporation and condensation of water are considered as a net substance flow rate into the liquid. The rate of evaporation and condensation are expressed as [75,45,44]

$$\dot{n}_{\text{eva}} = \frac{\alpha_M p_v^*}{W_{\text{H}_2\text{O}}\sqrt{2\pi R_v T_\infty}}, \tag{19}$$

and

$$\dot{n}_{\text{con}} = \frac{\alpha_M p_{\text{H}_2\text{O}}}{W_{\text{H}_2\text{O}}\sqrt{2\pi R_v T}}, \tag{20}$$

respectively. Here, $\alpha_M = 0.35$ [45] is the accommodation coefficient for the evaporation (assuming non-equilibrium phase change), p_v^* is the saturated vapour pressure, $W_{\text{H}_2\text{O}}$ is the molecular weight of water, R_v is the specific gas constant of water and $p_{\text{H}_2\text{O}}$ is the partial pressure of the vapour inside the bubble:

$$p_{\text{H}_2\text{O}} = X_{\text{H}_2\text{O}} \cdot p. \tag{21}$$

The quantities $\dot{n}_{\text{eva}}$ and $\dot{n}_{\text{con}}$ are representing the amount of evaporating and condensing moles of water in unit area and unit time, respectively. The difference of the two is the net evaporation rate, denoted simply by $\dot{n}_{\text{net}} (= \dot{n}_{\text{eva}} - \dot{n}_{\text{con}})$. The evaporation and condensation processes have a significant effect on the sonochemical behaviour since they considerably modify the amount of vapour trapped inside the bubble that can dissociate during the collapse phase and act as an effective third-body (see Sec. 2.2 for details). Keep in mind again that the physical part of the model is the same during each simulation; only the chemical mechanisms differ.

2.2. A state-of-the-art reaction mechanism for an oxygen bubble

The second part of the mathematical model primarily focuses on the chemical processes taking place inside the bubble. Here, an up-to-date, precisely validated reaction mechanism is presented that describes chemical processes inside an initially pure oxygen bubble. For a detailed description of the modelling approach with examples, the reader is referred to [76]. The major differences in the modelling technique between our and the three reaction mechanisms adopted form the literature for comparison is discussed in Sec. 2.4.

First, let us consider the following reversible chemical reactions involving K chemical species in the general form of

$$\sum_{k=1}^{K} \nu_{ki}^f \chi_k \Leftrightarrow \sum_{k=1}^{K} \nu_{ki}^b \chi_k \qquad (i = 1, \ldots, I), \tag{22}$$

where ν_{ki} are the stoichiometric coefficients, χ_k is the chemical symbol for the kth species, and I is the total number of reactions. The superscripts f and b indicate forward and backward directions, respectively. It is worth mentioning that most chemical reactions involve two or three species on each side of the chemical equation; hence, the matrices ν_{ki}^f and ν_{ki}^b are sparse, especially with increasing K.

Reaction kinetics focuses on the rate of chemical reactions. The net rate of reaction i (q_i) is calculated as the difference of forward and backward rates as

$$q_i = k_{f_i} \prod_{k=1}^{K} c_k^{\nu_{ki}^f} - k_{b_i} \prod_{k=1}^{K} c_k^{\nu_{ki}^b}, \tag{23}$$

where k_{f_i} and k_{b_i} are the forward and backward reaction rate constants of reaction i (defined later). With the reaction rates q_i, the production rate of each species can be written as

$$\dot{\omega}_k = \sum_{i=1}^{I} \nu_{ki} q_i, \qquad (k = 1, \ldots, K), \tag{24}$$

where $\nu_{ki} = \nu_{ki}^b - \nu_{ki}^f$. The production rate represents how fast the amount of species k changes in time in a unit volume.

With $\dot{\omega}_k$ being defined, the total net reaction heat, which was mentioned in Sec. 2.1, is

$$\dot{Q}_r = -\sum_{k=1}^{K} H_k \dot{\omega}_k. \tag{25}$$

With this term, the total heat transfer in Eq. (5) is

$$\sum \dot{Q} = \dot{Q}_{th} + \dot{Q}_r. \tag{26}$$

The forward rate coefficient k_{f_i}, used in Eq. (23) is calculated by the extended Arrhenius-equation written as

$$k_{f_i} = A_i T^{b_i} \exp\left(\frac{-E_i}{R_g T}\right), \tag{27}$$

where A_i is the pre-exponential factor, b_i is the temperature exponent, and E_i is the activation energy. The three constants (A_i, b_i and E_i) are different for each reactions, and they are fundamental inputs of a re-

action mechanism. The backward rate constants k_{b_i}—unlike in the referenced sonochemical articles—are calculated as follows. They are related to the forward rates through the equilibrium constant defined by

$$K_{c_i} = \frac{k_{f_i}}{k_{b_i}}. \tag{28}$$

The equilibrium constant K_{c_i} (given in molar concentration unit) can be determined as

$$K_{c_i} = K_{p_i}\left(\frac{P_{\text{atm}}}{R_g T}\right)^{\sum_{k=1}^{K}\nu_{ki}}, \tag{29}$$

where P_{atm} is the atmospheric pressure and K_{p_i} is obtained from

$$K_{p_i} = \exp\left(\frac{\Delta S_i}{R_g} - \frac{\Delta H_i}{R_g T}\right). \tag{30}$$

The notation Δ means the total change in a reaction (from reactants to products):

$$\frac{\Delta S_i}{R_g} = \sum_{k=1}^{K}\nu_{ki}\frac{S_k}{R_g}. \tag{31}$$

$$\frac{\Delta H_i}{R_g T} = \sum_{k=1}^{K}\nu_{ki}\frac{H_k}{R_g T}. \tag{32}$$

Here, S_k and H_k are the entropy and enthalpy of species k at temperature T, respectively. The exact values of the applied Arrhenius-coefficients are shown in Table A.7. The mechanism developed by Varga et al. [77] was extended with the O_3 reactions from [78] by Zhao et al. For detailed discussions of state-of-the-art $H_2/O_2/H_2O$ reaction mechanisms, the interested reader is referred to studies [79,80].

The Arrhenius-equation is a general approach for describing the temperature dependence of reaction rate coefficients; however, some chemical reactions behave in a more complex way, and their rate coefficients cannot be calculated with this function. This issue applies only to the forward rate coefficients; the backward rate coefficients are still calculated as described above. In the following, the three most important additional definitions are presented that are included in our modelling technique.

2.2.1. Three-body reactions

Thermally excited decomposition reactions require a so called third body collision partner, like

$$H_2O_2 + M \Leftrightarrow 2OH + M.$$

The collision with molecule M provides the excess energy for the H_2O_2 molecule needed for the decomposition. The collision partner M loses translational, rotational or vibrational energy, but does not change chemically. The so called complex bimolecular reactions also contain collision partner M, like in the reaction

$$H + O_2 + M \Leftrightarrow HO_2 + M.$$

The product of the collision of species H and O_2 is a highly energized product HO_2^*, which either decomposes, or loses energy via collision with M and is stabilized in the form of HO_2. In general, any molecule or radical can act as a third body, but the collision with larger molecules is more effective. This effect is taken into account in the third-body *collision efficiency factor* α_k, which has a unit value for N_2, smaller than 1 for O_2, and larger for bigger molecules. The third-body efficiency factor is very large for H_2O; $\alpha_{H_2O} = 12$ is assumed for several reactions. This means that considering the third-body efficiency factor of water is essential in sonochemistry where a large amount of water vapour is "trapped" inside the bubble during the rapid collapse. It is worth noting that the collision efficiency factors can be different in each reaction (even for the same component).

In a reaction equation, a third-body is marked with an additional M species on both sides, suggesting that the third-body does not take part in the reaction itself, for example:

In these cases, the reaction rate q_i obtained from Eq. (23) is modified as

$$q_i' = q_i[M], \tag{33}$$

where q_i' is the modified reaction rate, and

$$\left[M\right] = \sum_{k=1}^{K}\alpha_{ki}c_k, \tag{34}$$

is the effective total concentration of the third-body species and α_{ki} is the matrix of the third-body efficiency factors. The applied third-body efficiency factors are presented in Table A.8. Usually, most α_{ki} is assumed to be 1, and only those that differ from 1 are highlighted.

2.2.2. Pressure-dependent reactions

Some reaction rate constants are not only temperature, but also pressure-dependent. The phenomenon was first interpreted by Lindemann et al. [81] for the model reaction of cyclopropane isomerisation. Several later pieces of research confirmed the idea and extended the method for other areas in reaction kinetics [82–85]. Here, only a brief description of the *fall-off* reactions is presented; the interested reader is referred to the papers mentioned above.

A pressure-dependent reaction is marked with an M in brackets in the reaction equations:

$$H + O_2(+M) \Leftrightarrow HO_2(+M).$$

As a first step, the high-pressure limit (k_∞) and the low-pressure limit (k_0) rate coefficients have to be defined as

$$k_\infty = A_\infty T^{b_\infty}\exp\left(\frac{-E_\infty}{R_g T}\right), \tag{35}$$

$$k_0 = A_0 T^{b_0}\exp\left(\frac{-E_0}{R_g T}\right). \tag{36}$$

Consequently, there are two different sets of Arrhenius constants here. The two limiting rate constants together yield an overall rate constant using the equation

$$k_{f_i}' = k_\infty\frac{P_r}{1+P_r}F, \tag{37}$$

where the reduced pressure P_r is given by

$$P_r = \frac{k_0}{k_\infty}\left[M\right]. \tag{38}$$

Again, $[M]$ is the effective total concentration of the mixture enhanced by possible third-body efficiencies, calculated by Eq. (34). In Eq. (37), there are several approaches for the computation of F; here, only the *Troe* formalism [82] is introduced and employed:

$$\log F = \left[1 + \left[\frac{\log P_r + c}{n - d(\log P_r + c)}\right]^2\right]^{-1}\log F_{\text{cent}}, \tag{39}$$

with

$$c = -0.4 - 0.67\log F_{\text{cent}}, \tag{40}$$

$$n = 0.75 - 1.27\log F_{\text{cent}}, \tag{41}$$

$$d = 0.14, \tag{42}$$

and

$$F_{\text{cent}} = \left(1-\alpha\right)\exp\left(\frac{-T}{T^{***}}\right) + \alpha\exp\left(\frac{-T}{T^{*}}\right) + \exp\left(\frac{-T^{**}}{T}\right). \tag{43}$$

If T^{***} is very small (e.g. 10^{-30}) and T^{*} and T^{**} are very large (e.g. 10^{+30}), then Eq. (43) is reduced to $F_{\text{cent}} = \alpha$. This way a temperature independent F_{cent} value can be defined. From the equations above, it follows that (for a fall-off reaction)

$$k_{f_i}{}' \rightarrow \begin{cases} k_{\infty}, & \text{if } p \rightarrow \infty \\ k_0[M], & \text{if } p \rightarrow 0. \end{cases}$$

The four parameters α, T^{***}, T^{*} and T^{**} are different for each Troe-form reaction. In some cases, T^{**} is not used and the last term in Eq. (43) is neglected. In summary, ten parameters have to be defined for each pressure-dependent reaction using the Troe-formalism: six Arrhenius and four Troe coefficients. In most cases, these are extended with the corresponding third-body efficiency factors.

As an example, the rate constant of the pressure-dependent reaction

$$\mathrm{H + O_2\,(+M) \Leftrightarrow HO_2\,(+M)}$$

is depicted in Fig. 2 as a function of pressure at $T = 2000\ K$. Observe that the rate constant can vary between several orders of magnitude, suggesting that this effect is not negligible in sonochemistry.

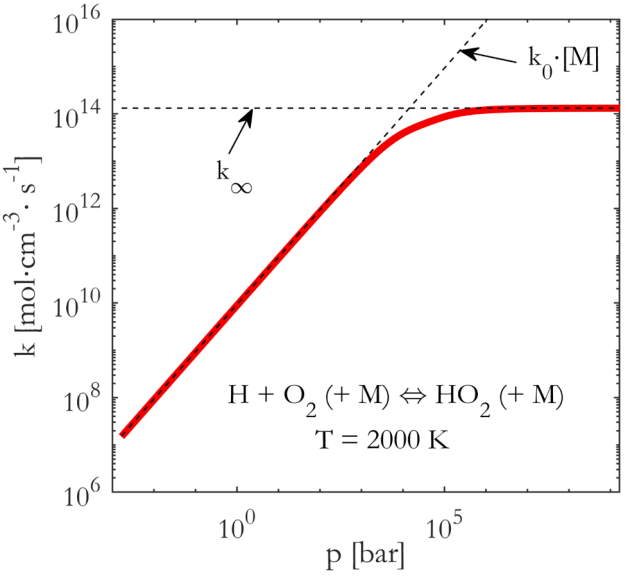

Fig. 2. The rate constant of the pressure-dependent reaction $\mathrm{H + O_2\,(+M) \Leftrightarrow HO_2\,(+M)}$ as a function of pressure at $T = 2000\ K$.

As a result of this procedure, the (modified) forward rate constant $k_{f_i}{}'$ can be determined. The backward reaction rate is calculated in the same way as in the case of the non-pressure-dependent reactions, see Eqs. (28)–(32). The employed low-pressure limit Arrhenius parameters and the Troe coefficients are summarized in Tables A.9 and A.10.

2.2.3. Duplicated reactions

Most elementary reactions occur via a single molecular mechanism and the temperature dependence of the rate constants of these reactions can be defined by a single set of Arrhenius parameters. In some rare cases, the reactants and products of an elementary reaction are identical, but the reaction proceeds via two different ways. The rate constants of these two channels have different temperature dependence; therefore, they can be characterised by two different sets of Arrhenius parameters. These reactions are given in the mechanisms as two separate reactions, like in the reaction

$$\mathrm{2HO_2 \Leftrightarrow O_2 + H_2O_2}$$

two Arrhenius-sets are defined:

$$\begin{aligned} A_1 &= 1.3000\cdot10^{11}\,\mathrm{cm^3/mol}, \quad b_1 = 0, \quad E_1 = -1.9983\cdot10^{3}\,\mathrm{cal/mol}, \\ A_2 &= 1.6048\cdot10^{15}\,\mathrm{cm^3/mol}, \quad b_2 = 0, \quad E_2 = +1.9063\cdot10^{4}\,\mathrm{cal/mol}. \end{aligned}$$

While calculating the reaction rates, the sum of the rates of the two channels is used as the rate of the reaction step. In Fig. 3, the rate constants of the above reaction are shown on normal scale (k vs. T, left panel) and on Arrhenius plot ($\log_{10}k$ vs. $1000/T$, right panel). It can be seen that for this reaction, the rate constant k_2 is dominant above 1500 K, the rate constant k_1 is dominant below 500 K, while both channels play an important role in the temperature range of 500 to 1500 K.

2.3. System of ordinary differential equations

The equation system to be resolved consists of the following ordinary differential equations (ODEs). Since the Keller–Miksis-equation defined by Eq. (1) is of second order, it represents two first-order ones. The first law of thermodynamics given via Eq. (5) is an ODE for the temporal evolution of the temperature (the pressure is acquired from the algebraic equation of the ideal gas law). The concentration change for each component is obtained from the production rates

$$\dot{c}_k = \dot{\omega}_k - c_k\frac{\dot{V}}{V}. \tag{44}$$

The concentration of water vapour is adjusted with the net evaporation rate as

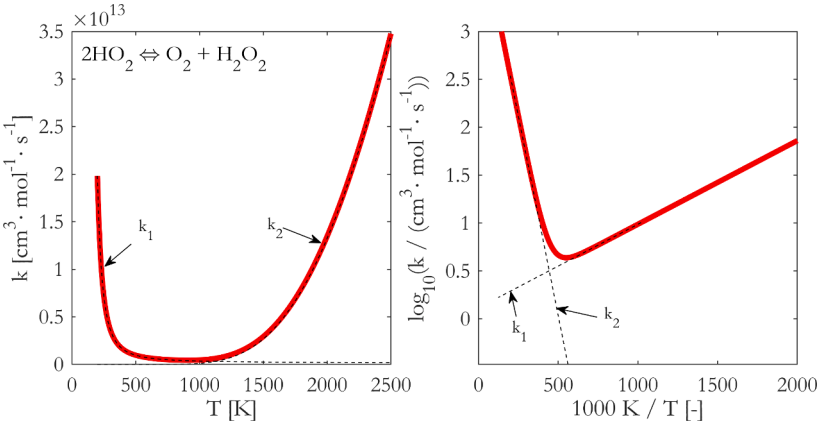

Fig. 3. The overall rate constant as a function of temperature for the duplicated reaction $\mathrm{2HO_2 \Leftrightarrow O_2 + H_2O_2}$. Left panel: k vs. T, right panel: $\log_{10}k$ vs. $1000/T$.

$$\dot{c}_{H_2O} = \dot{\omega}_{H_2O} - c_{H_2O}\frac{\dot{V}}{V} + \dot{n}_{net}\frac{A}{V}. \quad (45)$$

The dimension of the complete ODE system is $K + 3$, where the number of the chemical components is $K = 10$.

2.4. Comparison of the reaction mechanism with the ones frequently used in sonochemistry

For the sake of convenience, our chemical model described in Sec. 2.2 will be referred to as ELTE/HDS2022 throughout the rest of the paper. In this section, the differences between our model and three widely applied reaction mechanisms in the sonochemical literature is discussed briefly. All of these models have been used for bubbles containing initially only O_2 and water vapour. Our mechanism is considered as the most precise one, since it incorporates a realistic and detailed description of the chemical and physical processes occurring during the chemical reactions.

The first one was introduced by Kamath et al. [52] in 1993. This model was used and referenced several times by Lohse and Toegel [86,57] later in the following decades. It uses 19 different reaction equations and calculates the backward constants from distinct Arrhenius-equations with prescribed *backward* Arrhenius-constants. It does not include O_3 as a component. Several third-body efficiencies are indicated, but neither pressure-dependent nor duplicated reactions are used. The applied Arrhenius-constants are shown in the Appendix in Table B11. This mechanism is referred to as Kamath1993 later in this article.

The second model was applied by Yasui in some of his publications [47,48]. It uses 25 reactions and includes O_3 as a component. It also calculates the backward rate constants similarly to Kamath1993. Some third-body efficiencies are indicated; however, pressure-dependency and duplicated reactions are not taken into account. The applied Arrhenius-constants (including the rate parameters of the backward reactions) are summarised in Table B12. The model is indicated as Yasui2003.

The third mechanism is commonly used by Merouani and his co-workers in the last decades [67,62]. Rashwan in [87] also applies this model in his work. It consists of the same 19 reactions as in Kamath1993 with different Arrhenius-constants (they are different sometimes even by orders of magnitude). Here, O_3 is excluded in the model, and enhanced third-body efficiencies are not indicated; thus, they are regarded as 1 for all components. Again, pressure-dependence and duplicated reactions are not considered. The backward rate constants are estimated similarly to the first two models. The Arrhenius parameters for the forward and backward reactions are also shown in the Appendix (see Table B13). The mechanism is denoted as Merouani2014.

It must be noted that there are several other papers in the literature having different initial gas content. Their discussion is out of the scope of the present study. Nevertheless, it is to be stressed that to the best knowledge of the authors, they lack most of the advanced modelling principles introduced in Sec. 2.2.

3. Numerical methods and parameters

In our calculations, the ODE systems are solved with the Matlab built-in differential equation solver `ode15s`. It is a variable-step, variable-order numerical ODE solver of orders 1 to 5, with embedded error estimation. It is developed for solving stiff problems, which is certainly the case here (especially around the strong collapses). Both the relative and the absolute tolerances were set to 10^{-10} in all simulations.

The initial conditions are set as follows. The bubble is initiated from its equilibrium conditions; that is, from $R_0 = R_E, \dot{R}_0 = 0$ and $T_0 = T_\infty$, where R_E is the equilibrium bubble radius (bubble size) in the absence of ultrasonic irradiation. The specified value of R_E determines the initial pressure as $p_0 = P_\infty + 2\sigma/R_E$. The initial vapour content of the bubble is set according to the partial pressure of the saturated water vapour ($p_{H_2O,0} = p_v^*$), whereas the remaining oxygen content is set via $p_{O_2,0} = p_0 - p_{H_2O,0}$. This yields the initial concentration of oxygen and water vapour (in unit $mol \cdot m^{-3}$) to be

$$c_{O_2,0} = \frac{p_{O_2,0}}{R_g T_0}, \quad (46)$$

and

$$c_{H_2O,0} = \frac{p_{H_2O,0}}{R_g T_0}. \quad (47)$$

The initial concentration for every other component is 0 $mol \cdot m^{-3}$.

Each simulation was performed through 16 excitation cycles, and the first 12 of them are considered transient and got discarded. The last four cycles are regarded as convergent solution, and every further analysis is made on this convergent part. The 12 transient cycles seems to be short; however, when considerable amount of chemical reactions take place, the bubble have to exhibit strong collapse indicating large acoustic damping. Thus, in chemically relevant cases, this short initial transient is reasonable.

The fixed physical parameters (material and ambient properties) during the simulations are shown in Table 1. The values of the control parameters (p_A, f and R_E) are given in Table 2. The total number of parameter combinations is $41 \cdot 6 \cdot 2 = 492$. Therefore, all the four models were simulated 492 times. The computational time for each equilibrium radius was around 12 h on a 4 threaded Intel Core i7-4790 CPU @ 3.60 GHz.

Table 1
The applied physical constants during the simulations.

Name	Abbrev.	Value	Unit
Liquid sound speed	c_L	1483	m/s
Liquid density	ρ_L	998.2	kg/m^3
Surface tension	σ	$71.97 \cdot 10^{-3}$	N/m
Dynamic viscosity	μ_L	0.001	Pa·s
Ambient pressure	P_∞	1	bar
Ambient temperature	T_∞	300	K
Univ. gas constant	R_g	8.31446	J/mol·K
Accommodation coeff. for evaporation	α_M	0.35	–
Saturated vapour pressure	p_v^*	2338.1	Pa

Table 2
The ranges of the control parameters. The total number of parameter combinations is 492.

Parameter name	Abbrev.	Value range
Pressure amplitude	p_A	1 to 2 bar, increment: 0.025 bar
Ultrasound frequency	f	20, 35, 50, 75, 100, 200 kHz
Equilibrium radius	R_E	$4, 8\,\mu m$
	Corresponding natural frequency, f_n	912.6, 430.6 kHz

4. Comparison of the reaction mechanisms via the chemical yield

Performing a simulation with the conditions mentioned above, one can obtain the time curves of bubble radius, bubble wall velocity, internal temperature, and the concentration of each component.

The convergent time curves (last four acoustic cycles) at $p_A = 1.8\,\text{bar}$, $f = 100\,\text{kHz}$ and $R_E = 8\,\mu\text{m}$ with the ELTE/HDS2022 model are shown in Fig. 4. On the top chart, the dimensionless bubble radius (R/R_E) is drawn with blue, and the internal temperature with red lines, respectively. On the bottom chart, the amount of substance for each component (n_k) are shown in moles with different colors on logarithmic scale. Notice that the time axes are in dimensionless form of $\tau = t{\cdot}f$ in both cases, resulting in $\tau = 1$ being one excitation cycle.

It is apparent from the time curves that during the violent collapses, the internal temperature grows significantly, even up to over 4000 K. The main reason for this is that the time scale of heat transfer between the liquid and the bubble interior is considerably larger than the duration of the collapse; thus, the cooling effect cannot compensate the extreme amount of work done by the rapid compression. In the relatively slow expansion phase; however, heat diffusion balances out the expansion work, and the internal temperature does not vary from the ambient temperature remarkably.

During the expansion phase, only the molecule number of the water vapour changes noticeably due to the high rate of evaporation from the liquid. At the strong collapses, the immense peak temperature induces the dissociation of the accumulated water vapour. As a result, the amount of water vapour decreases drastically, and the molecule number of other products (such as H, H_2, HO_2 and many others) start to rise rapidly. However, after the really short collapse time, the temperature drops back roughly to the ambient temperature, and the dissociation of water vapour stops. Consequently, the amount of the aforementioned products slightly decreases (due to recombination processes), and after the possible afterbounces, they stay constant through the subsequent expansion phase. This process repeats itself in each excitation cycle. In the long run, the bubble pulsates identically through several cycles, maintaining this dynamical equilibrium.

In order to quantify the chemical activity of the bubble, a proper definition of the chemical output is required. Several different definitions of the chemical yield have been introduced during the last decades, each for its own objective (i.e. maximum number of molecules [48,87], or the total diffusing molecules out of the bubble [39], etc.). In the present study, for keeping simplicity, the chemical yield for each component is defined as *the amount of substance in moles at the maximum bubble radius* taken at the convergent integration phase. This approach is useful from a practical point of view: by turning off the ultrasonic irradiation, the bubble most likely contains this amount of substance. In this way, the fluctuations caused by the possible afterbounces are also taken into account. An example is presented in Fig. 4, where the vertical dashed black line indicates the maximum bubble radius. Its intersection with the corresponding molecule amounts are the investigated chemical yields of the components, see the arrows on the bottom chart.

4.1. Pressure amplitude response curves

After performing the simulations, one can obtain the chemical yields for every component at a given parameter combination. The evaluation strategy is to compare the chemical yield of several components at various control parameter values for the four chemical models introduced in Sec. 2.4.

For instance, Fig. 5 shows the yield of hydrogen as a function of p_A with $R_E = 8\,\mu\text{m}$ at 4 different driving frequencies (20, 50, 100 and 200 kHz). Note that the vertical axes are on logarithmic scale. Hydrogen is of keen interest in sonochemistry and its production has become a very appealing topic lately [88,87,89]. It is apparent that the chemical yield intensifies radically at around $p_A = 1 - 1.4\,\text{bar}$ (where the threshold for sonochemical activity is reached) with all four models. Moreover, increasing the driving frequency shifts this sonochemical threshold to higher pressure amplitudes.

In some certain parameter domains, fairly good quantitative agreement can be observed between the models considering the hydrogen outcome. For example, at $f = 20\,\text{kHz}$, from $p_A = 1.1$ to $1.5\,\text{bar}$, all the other three models agree quite well with ELTE/HDS2022. However, the yield with ELTE/HDS2022 has a maximum value at around $p_A = 1.5\,\text{bar}$, and it starts to decrease slightly above. An overall good agreement can be found between Kamath1993 and ELTE/HDS2022, especially at $f = 50$

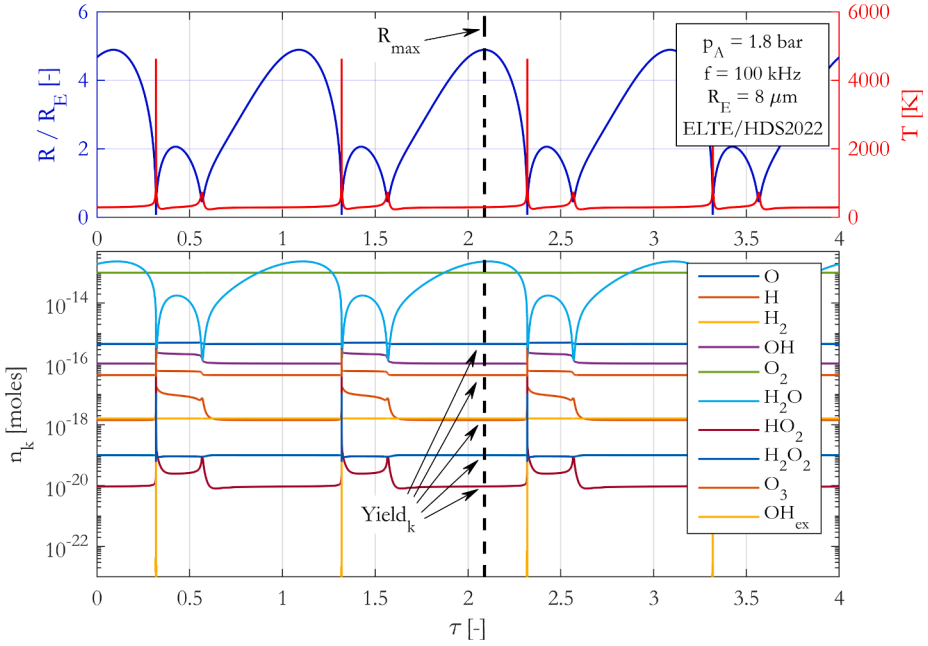

Fig. 4. The convergent time curves at $p_A = 1.8\,\text{bar}$, $f = 100\,\text{kHz}$ and $R_E = 8\,\mu\text{m}$ with the ELTE/HDS2022 model. On the top chart, the dimensionless bubble radius is shown with blue line, and the temperature with red line. On the bottom chart, the amounts of substance are drawn for the different components on logarithmic scale. The time axes are also in dimensionless form.

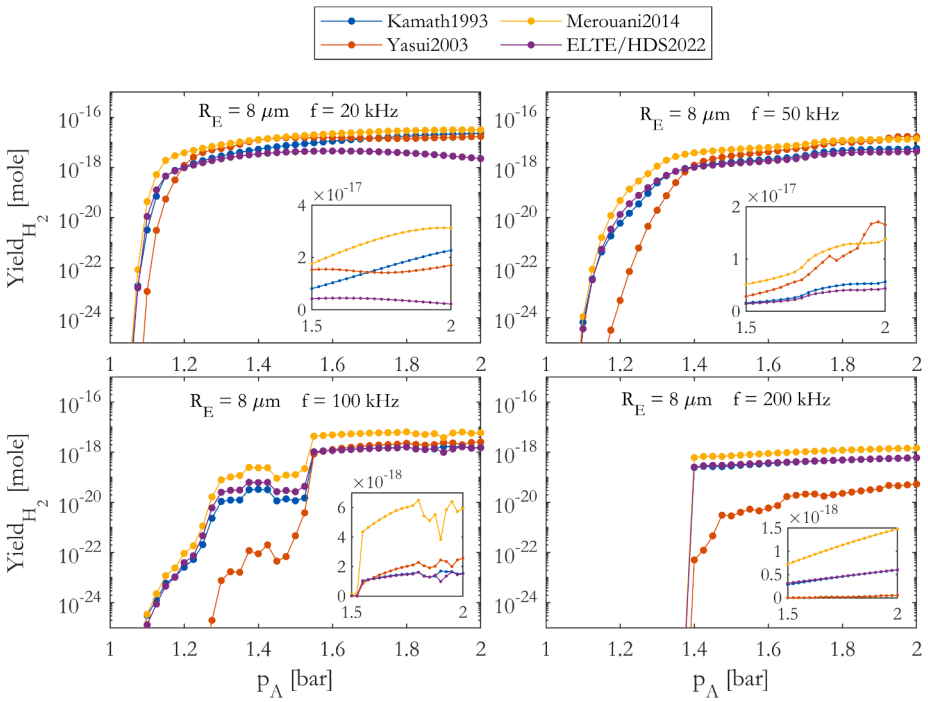

Fig. 5. The chemical yield of H_2 as a function of the pressure amplitude at $R_E = 8\,\mu$m, at four different driving frequencies. The graphs are magnified on a linear scale from $p_A = 1.5 - 2$ bar.

and 200 kHz but Merouani2014 also follows their trend moderately well. Only Yasui2003 differs significantly from the other three mechanisms, particularly at higher driving frequencies. However, keep in mind that the yield axes are on logarithmic scale, meaning even a small distance in the graphs can mean 2-3-fold difference in numerical values (the graphs are magnified on linear scales on the bottom right of the charts). Nevertheless, regarding H_2 outcome, it can be stated that the four examined models behave in a similar way.

Despite of the relatively good agreement between the reaction mechanisms for hydrogen production, *large variance emerges* for *almost all other components*. For example, in the case of H_2O_2, the same graphs are shown in Fig. 6 as in the case of Fig. 5, except at $R_E = 4\,\mu$m. Hydrogen peroxide is used especially in wastewater technologies [90], and several experimental works focus on its production [14,91]. *The discrepancy amongst the models is more than apparent: the numerical values tend to differ by up to more than two orders of magnitude, and even the trends of the yields can vary drastically.* Observe, for example, that the yield of Kamath1993 is almost 100 times higher than that of Merouani2014, and

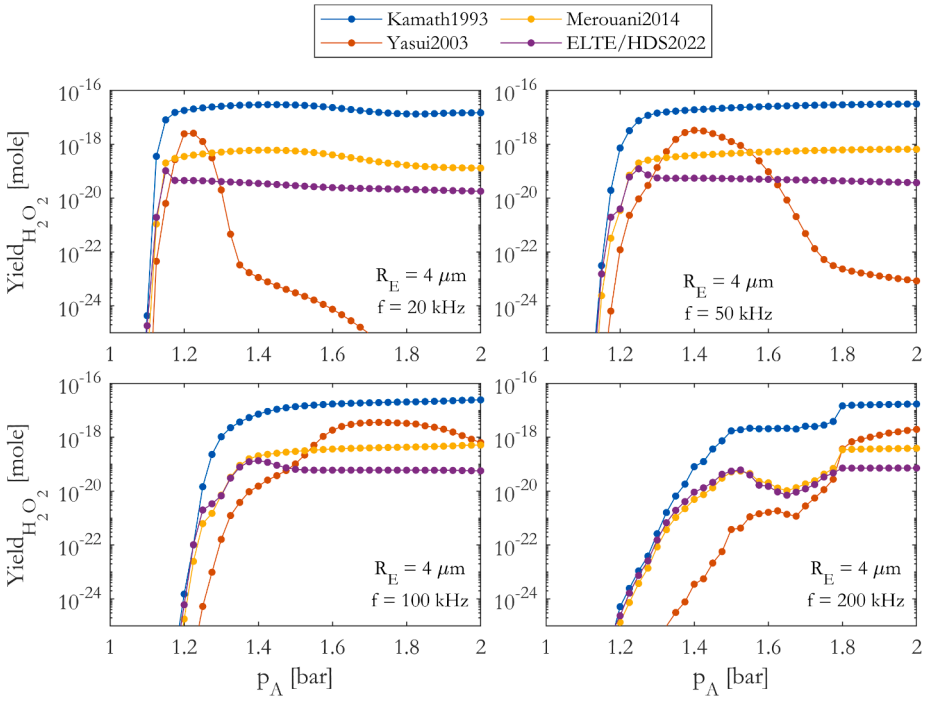

Fig. 6. The chemical yield of H_2O_2 as a function of the pressure amplitude at $R_E = 4\,\mu$m, at four different driving frequencies.

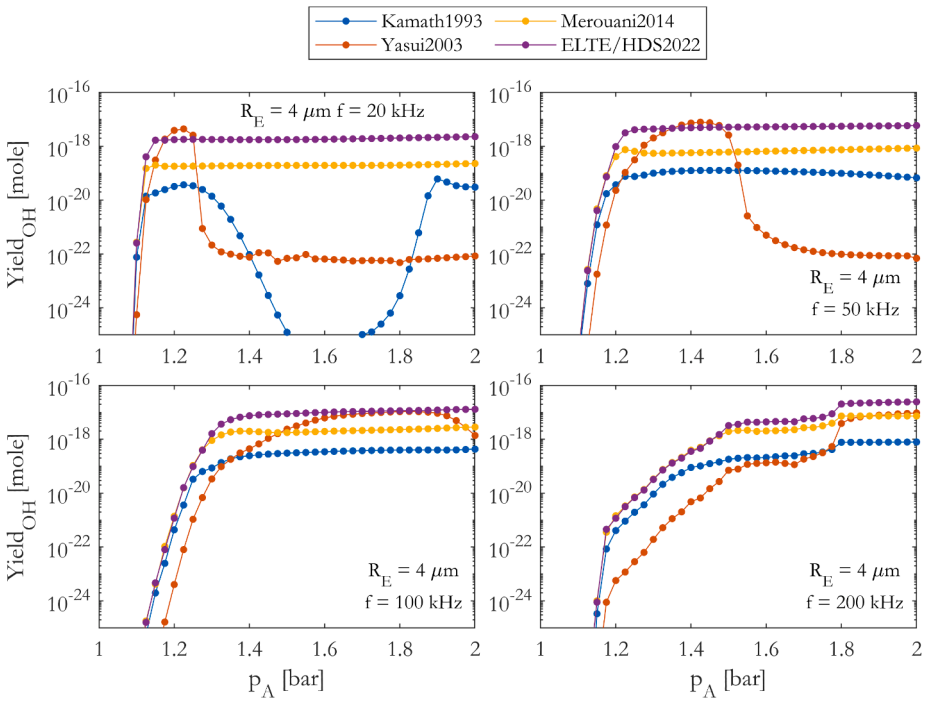

Fig. 7. The chemical yield of OH radical as a function of the pressure amplitude at $R_E = 4\mu$m, at four different driving frequencies.

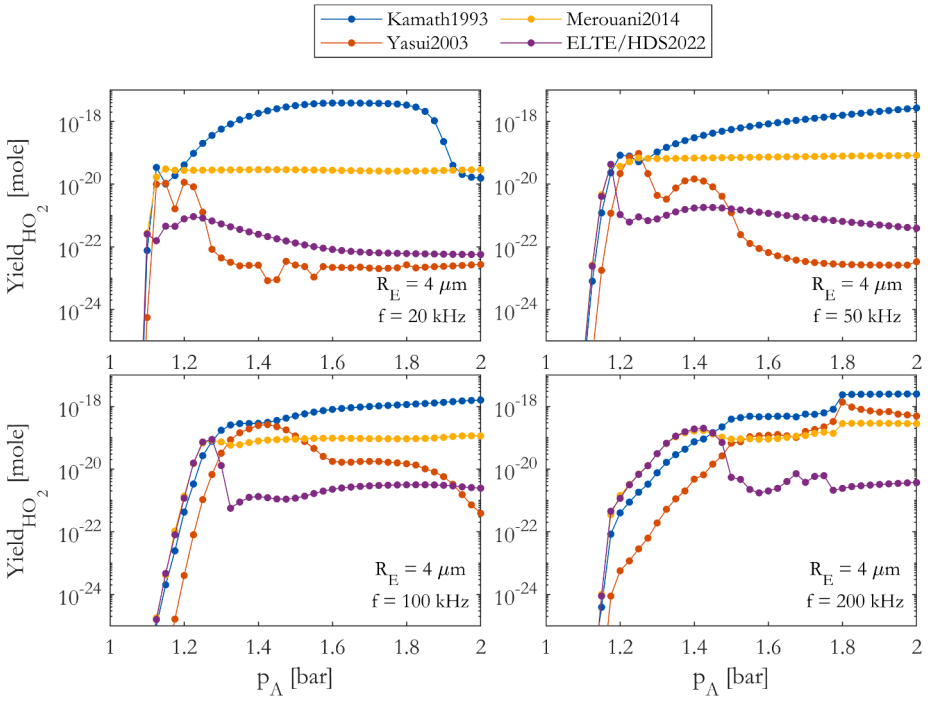

Fig. 8. The chemical yield of HO_2 as a function of the pressure amplitude at $R_E = 4\mu$m, at four different driving frequencies.

even bigger than that of ELTE/HDS2022. The model of Yasui2003 behaves even qualitatively differently than the other three; it shows a visible peak of H_2O_2 yield at lower pressure amplitude values for all driving frequencies, followed by a steep decrease as p_A increases (except for $f = 200$ kHz). This can lead to the identification of false optimal operating conditions.

Similar behaviour can be seen for the other strong oxidants, for example OH radical or HO_2, as well. Their respective yields are shown at $R_E = 4\mu$m in Figs. 7 and 8. The orders of magnitude differences are clearly visible, and the trends also differ between the mechanisms. Observe, for example, the deep "valley" in OH yield (Fig. 7) with Kamath1993 at $f = 20$ kHz, or the peaks with Yasui2003 at $f = 20-100$ kHz, which are absent in the cases of Merouani2014 and ELTE/HDS2022. Although the variances somewhat diminish with increasing driving frequency, quantitative agreement can hardly be identified.

The biggest difference can be observed in the case of HO_2 yield (Fig. 8). Kamath1993 shows a monotonously increasing yield with the pressure amplitude at all frequencies, except for $f = 20$ kHz over $p_A = 1.8$ bar. The yield with Merouani2014 remains rather constant, especially at $f = 20-100$ kHz, while ELTE/HDS2022 and Yasui2003 have their

maximum yields at relatively low pressure amplitudes (around $p_A \approx 1.2-1.4$ bar); but their trends are very dissimiliar. At $f = 200$ kHz, the yields of ELTE/HDS2022 differs by almost two orders of magnitude from the other three models.

4.2. Quantitative comparison of the mechanisms

For a more thorough comparison of the reaction mechanisms, the yields of all the chemical components have to be taken into account. In order to avoid the plot of a large number of figures, the yields are compared only at two parameter combinations: $R_E = 4\,\mu$m, $p_A = 2$ bar, $f = 50$ kHz (Case 1, Table 3) and $R_E = 8\,\mu$m, $p_A = 2$ bar, $f = 100$ kHz (Case 2, Table 4).

It is apparent from the tables that in some rare cases, a fairly good numerical agreement can be found between the models. Compare, for example, the yields of OH in Case 1, where the values for Merouani2014 and ELTE/HDS2022 are rather similar ($8.5293\cdot10^{-19}$ and $2.2682\cdot10^{-18}$ mol highlighted by bold text in the table). Keep in mind that it is still almost a three fold difference between the yields. The other two models differ from these values by orders of magnitude. Relatively good agreement can also be observed in Case 2 for the H_2 output; for all the four models they are in the same order of magnitude (as it was already pointed out in Sec. 4.1).

However, comparing only a single component at a specific parameter combination can be misleading in the understanding of the complete picture. In spite of the good agreement between Merouani2014 and ELTE/HDS2022 for the production of hydrogen molecules in Case 2, the H_2O_2 output differs by a factor of 21. In addition, the crossing pressure amplitude response curves (see for instance Fig. 8, at $f = 20$ kHz) indicate that a parameter combination usually exists where two reaction mechanisms provide nearly the same yields for a specific component. This does not imply that good agreement holds for a wide range of parameters and/or for another component (see again Figs. 6–8). In general, from the values presented in Tables 3 and 4, it is clear that the calculated chemical yields usually differ by several orders of magnitudes; thus, the proper modelling of the chemical reactions is mandatory for drawing meaningful conclusions.

Table 3
The chemical yield of several components with the four models at $R_E = 4\,\mu$m, $p_A = 2$ bar and $f = 50$ kHz (Case 1).

Component	Yield [mole]			
	Kamath1993	Yasui2003	Merouani2014	ELTE/HDS2022
O	$7.4819\cdot10^{-20}$	$6.6699\cdot10^{-16}$	$6.4846\cdot10^{-18}$	$5.3582\cdot10^{-17}$
H	$1.4769\cdot10^{-22}$	$2.9508\cdot10^{-16}$	$8.5419\cdot10^{-19}$	$5.377\cdot10^{-20}$
H_2	$3.2419\cdot10^{-18}$	$1.8631\cdot10^{-17}$	$4.3697\cdot10^{-18}$	$3.4358\cdot10^{-19}$
OH	$6.7356\cdot10^{-20}$	$6.9494\cdot10^{-23}$	**$8.5293\cdot10^{-19}$**	**$2.2682\cdot10^{-18}$**
HO_2	$2.6952\cdot10^{-18}$	$3.3472\cdot10^{-23}$	$8.2519\cdot10^{-20}$	$5.7095\cdot10^{-23}$
H_2O_2	$3.1168\cdot10^{-17}$	$8.4383\cdot10^{-24}$	$6.516\cdot10^{-19}$	$1.8041\cdot10^{-20}$
O_3	0	$1.1771\cdot10^{-23}$	0	$5.4264\cdot10^{-19}$

Table 4
The chemical yield of several components with the four models at $R_E = 8\,\mu$m, $p_A = 2$ bar and $f = 100$ kHz (Case 2).

Component	Yield [mole]			
	Kamath1993	Yasui2003	Merouani2014	ELTE/HDS2022
O	$3.7912\cdot10^{-17}$	$1.4461\cdot10^{-17}$	$9.811\cdot10^{-17}$	$3.4092\cdot10^{-16}$
H	$2.6629\cdot10^{-19}$	$2.4684\cdot10^{-17}$	$1.6617\cdot10^{-17}$	$3.4843\cdot10^{-19}$
H_2	**$1.5451\cdot10^{-18}$**	**$2.566\cdot10^{-18}$**	**$5.9448\cdot10^{-18}$**	**$2.2287\cdot10^{-18}$**
OH	$4.2084\cdot10^{-18}$	$6.3705\cdot10^{-17}$	$3.402\cdot10^{-17}$	$1.5793\cdot10^{-17}$
HO_2	$9.1965\cdot10^{-18}$	$4.9736\cdot10^{-19}$	$9.5032\cdot10^{-19}$	$1.8663\cdot10^{-22}$
H_2O_2	$7.4967\cdot10^{-17}$	$7.7173\cdot10^{-18}$	$7.9393\cdot10^{-19}$	$3.7281\cdot10^{-20}$
O_3	0	$2.5344\cdot10^{-17}$	0	$1.9318\cdot10^{-18}$

5. Summary and discussion

The present study focuses on the chemical modelling of single-bubble sonochemistry. A detailed, state-of-the-art chemical mechanism is presented for a bubble initially containing only oxygen and water vapour. The model includes accurately validated Arrhenius-coefficients and third-body efficiency factors, takes into account pressure-dependent and duplicated reactions, and calculates the backward rate constants from accurate equilibrium equations.

The proposed mechanism was compared to three other chemical models that are widely used in sonochemistry (only the reaction mechanisms were different). The analysis is made via a well-defined chemical output. Apart from some moderately good agreements in some cases, it was shown that there are orders of magnitude differences between the yields of the products as calculated from the various chemical models in a wide parameter range. In addition, the trends of the yield as a function of control parameters can have different characteristics; thus, one can identify false optimal operating conditions.

The immense amount of differences between the results have various reasons. Obviously, the difference in the Arrhenius-coefficients can lead to large differences in the rate constants due to the strong exponential dependence on the temperature. The effect of pressure-dependency and reaction duplication may also have a high impact in sonochemical applications since the peak pressure can lead up to even several hundreds of bars during the strong collapse. This can cause substantial change in rate constant of pressure-dependent reactions. As already mentioned before in Sec. 2.2, the effect of third-body efficiencies is also important in a gas mixture where water vapour has very high concentration.

These imply that in order to make qualitatively and quantitatively correct conclusions about the chemical activity, *it is mandatory to employ an up-to-date, properly validated chemical mechanism* for a given sonochemical task.

Declaration of Competing Interest

The authors declare the following financial interests/personal relationships which may be considered as potential competing interests: Csanád Kalmár reports financial support was provided by Ministry of Human Capacities. Tamás Turányi reports financial support was provided by Hungarian National Research, Development and Innovation Office. Ferenc Hegedűs reports financial support was provided by Ministry of Innovation and Technology of Hungary. Ferenc Hegedűs reports financial support was provided by Hungarian Academy of Sciences.

Acknowledgements

The authors acknowledge the financial support of the Hungarian National Research, Development and Innovation Office via NKFIH grant OTKA K132109.

The research reported in this paper is part of project No. BME-NVA-02, implemented with the support provided by the Ministry of Innovation and Technology of Hungary from the National Research, Development and Innovation Fund, financed under the TKP2021 funding scheme.

The research was also supported by the ÚNKP-20–3-II New National Excellence Program of the Ministry of Human Capacities, and by the János Bolyai Research Scholarship of the Hungarian Academy of Sciences.

Appendix A. Data tables for the applied chemical mechanism

See Tables A.5–A.10.

Table A.5
The thermodynamic properties of each species.

Component	$W\left[\frac{\mathrm{g}}{\mathrm{mol}}\right]$	T_{low} [K]	T_{mid} [K]	T_{high} [K]	$\lambda_k\left[\frac{\mathrm{W}}{\mathrm{mK}}\right]$
O	16	200	1000	6000	–
H	1	200	1000	6000	–
H_2	2	200	1000	6000	0.1805
OH	17	200	1000	6000	–
O_2	32	200	1000	6000	0.02658
H_2O	18	200	1000	6000	0.016
HO_2	33	200	1000	5000	–
H_2O_2	34	200	1000	6000	0.5863
O_3	48	200	1000	6000	–
OH_{ex}	17	300	1000	5000	–

Table A.6
The applied NASA coefficients of each species, taken from [77,78]. The units of the coefficients set the units of $C_{p,k}, H_k$ and S_k values in Eqs. (6)–(8) to be in CGS unit system.

Component		NASA coefficients						
		a_1	a_2	a_3	a_4	a_5	a_6	a_7
O	low	3.1683	$-3.2793\cdot10^{-3}$	$6.6431\cdot10^{-6}$	$-6.1281\cdot10^{-9}$	$2.1127\cdot10^{-12}$	$2.9122\cdot10^{4}$	2.0519
	high	2.5436	$-2.7316\cdot10^{-5}$	$-4.1903\cdot10^{-9}$	$4.9548\cdot10^{-12}$	$-4.7955\cdot10^{-16}$	$2.9226\cdot10^{4}$	4.9223
H	low	2.5	0	0	0	0	$2.5474\cdot10^{4}$	$-4.4668\cdot10^{-1}$
	high	2.5	0	0	0	0	$2.5474\cdot10^{4}$	$-4.4668\cdot10^{-1}$
H_2	low	2.3443	$7.9805\cdot10^{-3}$	$-1.9478\cdot10^{-5}$	$2.0157\cdot10^{-8}$	$-7.3761\cdot10^{-12}$	$-9.1794\cdot10^{2}$	$6.8301\cdot10^{-1}$
	high	2.9329	$8.2661\cdot10^{-4}$	$-1.464\cdot10^{-7}$	$1.541\cdot10^{-11}$	$-6.888\cdot10^{-16}$	$-8.1307\cdot10^{2}$	−1.0243
OH	low	3.992	$-2.4011\cdot10^{-3}$	$4.6166\cdot10^{-6}$	$-3.8792\cdot10^{-9}$	$1.3632\cdot10^{-12}$	$3.3689\cdot10^{3}$	$-1.04\cdot10^{-1}$
	high	2.8385	$1.1074\cdot10^{-3}$	$-2.94\cdot10^{-7}$	$4.207\cdot10^{-11}$	$-2.4229\cdot10^{-15}$	$3.6978\cdot10^{3}$	5.8449
O_2	low	3.7825	$-2.9967\cdot10^{-3}$	$9.8473\cdot10^{-6}$	$-9.6813\cdot10^{-9}$	$3.2437\cdot10^{-12}$	$-1.0639\cdot10^{3}$	3.6577
	high	3.661	$6.5637\cdot10^{-4}$	$-1.4115\cdot10^{-7}$	$2.058\cdot10^{-11}$	$-1.2991\cdot10^{-15}$	$-1.216\cdot10^{3}$	3.4154
H_2O	low	4.1986	$-2.0364\cdot10^{-3}$	$6.5203\cdot10^{-6}$	$-5.4879\cdot10^{-9}$	$1.772\cdot10^{-12}$	$-3.0294\cdot10^{4}$	$-8.4901\cdot10^{-1}$
	high	2.677	$2.9732\cdot10^{-3}$	$-7.7377\cdot10^{-7}$	$9.4434\cdot10^{-11}$	$-4.269\cdot10^{-15}$	$-2.9886\cdot10^{4}$	6.8826
HO_2	low	4.3018	$-4.7491\cdot10^{-3}$	$2.1158\cdot10^{-5}$	$-2.4276\cdot10^{-8}$	$9.2923\cdot10^{-12}$	$2.6402\cdot10^{2}$	3.7167
	high	4.1723	$1.8812\cdot10^{-3}$	$-3.4628\cdot10^{-7}$	$1.9466\cdot10^{-11}$	$1.7626\cdot10^{-16}$	31.0207	2.9577
H_2O_2	low	4.3152	$-8.4739\cdot10^{-4}$	$1.764\cdot10^{-5}$	$-2.2676\cdot10^{-8}$	$9.0895\cdot10^{-12}$	$-1.7707\cdot10^{4}$	3.2737
	high	4.5798	$4.0533\cdot10^{-3}$	$-1.2984\cdot10^{-6}$	$1.9821\cdot10^{-10}$	$-1.1397\cdot10^{-14}$	$-1.8007\cdot10^{4}$	$6.6497\cdot10^{-1}$
O_3	low	3.4074	$2.0538\cdot10^{-3}$	$1.3849\cdot10^{-5}$	$-2.2331\cdot10^{-8}$	$9.7607\cdot10^{-12}$	$1.5864\cdot10^{4}$	8.2825
	high	12.3303	$-1.1932\cdot10^{-2}$	$7.9874\cdot10^{-6}$	$-1.7719\cdot10^{-9}$	$1.2608\cdot10^{-13}$	$1.2676\cdot10^{4}$	−40.8823
OH_{ex}	low	3.6373	$1.8509\cdot10^{-4}$	$-1.6762\cdot10^{-6}$	$2.3872\cdot10^{-9}$	$-8.4314\cdot10^{-13}$	$5.0021\cdot10^{4}$	1.3589
	high	2.8827	$1.014\cdot10^{-3}$	$-2.2769\cdot10^{-7}$	$2.1747\cdot10^{-11}$	$-5.1263\cdot10^{-16}$	$5.0265\cdot10^{4}$	5.5957

Table A.7
The applied chemical mechanism with their Arrhenius-constants. The values are taken from [77,78]. For pressure dependent reactions marked with (+M), the values A_i, b_i and E_i represent the coefficients A_∞, b_∞ and E_∞, respectively. The units for A_i are in $1/\mathrm{s}$ for first order reactions, and in $\mathrm{cm}^3/\mathrm{mol}\cdot\mathrm{s}$ for second order reactions. The units for E_i are in cal/mol. For the rest of the special coefficients, see Tables A.8, A.9, A.10.

No.	Reaction	A_i	b_i	E_i
1.	$H + OH + M \Leftrightarrow H_2O + M$	$1.4818\cdot10^{24}$	−2.5379	$1.4808\cdot10^{2}$
2.	$2O + M \Leftrightarrow O_2 + M$	$6.165\cdot10^{15}$	−0.5	0
3.	$O + H + M \Leftrightarrow OH + M$	$4.714\cdot10^{18}$	−1	0
4.	$H + O_2 \Leftrightarrow O + OH$	$5.0712\cdot10^{15}$	−0.48596	$1.9771\cdot10^{4}$
5.	$H + O_2 (+ M) \Leftrightarrow HO_2 (+ M)$	$4.65\cdot10^{12}$	0.44	0
6.	$2OH \Leftrightarrow O + H_2O$	$8.4999\cdot10^{4}$	2.2642	$-2.1881\cdot10^{3}$
7.	$H + HO_2 \Leftrightarrow H_2 + O_2$	$2.1231\cdot10^{6}$	2.1133	$-1.9919\cdot10^{3}$
8.	$H + HO_2 \Leftrightarrow 2OH$	$5.7734\cdot10^{13}$	0	$2.0967\cdot10^{2}$
9.	$O + HO_2 \Leftrightarrow OH + O_2$	$3.25\cdot10^{13}$	0	0
10.	$OH + HO_2 \Leftrightarrow O_2 + H_2O$	$9.584\cdot10^{11}$	0.42008	$-1.1629\cdot10^{3}$
11.	$2H + M \Leftrightarrow H_2 + M$	$4.9806\cdot10^{18}$	−1.2127	$7.5034\cdot10^{2}$
12.	$O + H_2 \Leftrightarrow H + OH$	$1.2554\cdot10^{6}$	2.2704	$8.5289\cdot10^{3}$

(continued on next page)

Table A.7 (*continued*)

No.	Reaction	A_i	b_i	E_i
13.	$H_2 + OH \Leftrightarrow H + H_2O$	$1.3193 \cdot 10^7$	1.878	$3.863 \cdot 10^3$
14.	$2OH\ (+\ M) \Leftrightarrow H_2O_2\ (+\ M)$	$2.148 \cdot 10^5$	2.3219	$-4.1712 \cdot 10^3$
15.	$H + H_2O_2 \Leftrightarrow OH + H_2O$	$2.41 \cdot 10^{13}$	0	$4.8671 \cdot 10^3$
16.	$H + H_2O_2 \Leftrightarrow H_2 + HO_2$	$9.7543 \cdot 10^{19}$	−1.9249	$1.1555 \cdot 10^4$
17.	$O + H_2O_2 \Leftrightarrow OH + HO_2$	$9.55 \cdot 10^6$	2	$4.8671 \cdot 10^3$
18.	$OH + H_2O_2 \Leftrightarrow H_2O + HO_2$ (dupl.)	$1.74 \cdot 10^{12}$	0	$3.8986 \cdot 10^2$
19.		$7.59 \cdot 10^{13}$	0	$8.9116 \cdot 10^3$
20.	$2HO_2 \Leftrightarrow O_2 + H_2O_2$ (dupl.)	$1.3 \cdot 10^{11}$	0	$-1.9983 \cdot 10^3$
21.		$1.6048 \cdot 10^{15}$	0	$1.9063 \cdot 10^4$
22.	$O_3\ (+\ M) \Leftrightarrow O + O_2\ (+\ M)$	$1.37 \cdot 10^{15}$	−0.67	$2.599 \cdot 10^4$
23.	$H + O_3 \Leftrightarrow OH + O_2$	$8.43 \cdot 10^{13}$	0	$9.34 \cdot 10^2$
24.	$H + O_3 \Leftrightarrow O + HO_2$	$4.52 \cdot 10^{11}$	0	0
25.	$OH + O_3 \Leftrightarrow O_2 + HO_2$	$1.85 \cdot 10^{11}$	0	$8.31 \cdot 10^2$
26.	$HO_2 + O_3 \Leftrightarrow OH + 2O_2$	$6.62 \cdot 10^9$	0	$9.94 \cdot 10^2$
27.	$O + O_3 \Leftrightarrow 2O_2$	$4.82 \cdot 10^{12}$	0	$4.094 \cdot 10^3$
28.	$H_2O + O_3 \Leftrightarrow O_2 + H_2O_2$	66.2	0	0
29.	$O + H + M \Leftrightarrow OH_{ex} + M$	$1.5 \cdot 10^{13}$	0	$7.3252 \cdot 10^3$
30.	$H_2O + OH_{ex} \Leftrightarrow OH + H_2O$	$5.93 \cdot 10^{12}$	0.5	$-1.0543 \cdot 10^3$
31.	$H_2 + OH_{ex} \Leftrightarrow H_2 + OH$	$2.95 \cdot 10^{12}$	0.5	$-5.4432 \cdot 10^2$
32.	$OH + OH_{ex} \Leftrightarrow 2OH$	$6.01 \cdot 10^{12}$	0.5	$-9.3664 \cdot 10^2$
33.	$H + OH_{ex} \Leftrightarrow H + OH$	$1.31 \cdot 10^{12}$	0.5	$-2.0475 \cdot 10^2$
34.	$O_2 + OH_{ex} \Leftrightarrow OH + O_2$	$2.1 \cdot 10^{12}$	0.5	$-5.86 \cdot 10^2$

Table A.8
The enhanced third-body efficiencies. For every other non-mentioned component, $\alpha_{k,i} = 1$.

No.	Reaction	Enhanced third-body efficiencies ($\alpha_{k,i}$)
1.	$H + OH + M \Leftrightarrow H_2O + M$	H_2: 2.5 H_2O: 12
2.	$2O + M \Leftrightarrow O_2 + M$	H_2: 2.5 H_2O: 12
3.	$O + H + M \Leftrightarrow OH + M$	H_2: 2.5 H_2O: 12
5.	$H + O_2\ (+\ M) \Leftrightarrow HO_2\ (+\ M)$	H_2: 1.511 H_2O: 11.372
11.	$2H + M \Leftrightarrow H_2 + M$	H_2: 2.5 H_2O: 12
14.	$2OH\ (+\ M) \Leftrightarrow H_2O_2\ (+\ M)$	H_2: 2.47 O_2: 0.8 H_2O: 5 H_2O_2: 5.13
22.	$O_3\ (+\ M) \Leftrightarrow O + O_2\ (+\ M)$	O: 6 H_2: 3 O_2: 1.5 O_3: 3.75
29.	$O + H + M \Leftrightarrow OH_{ex} + M$	O_2: 0.4 H_2O: 6.5

Table A.9
The low-pressure limit Arrhenius parameters of the pressure-dependent reactions. The units for A_0 are in $1/s$ for first order reactions, and in $cm^3/mol \cdot s$ for second order reactions. The units for E_0 are in cal/mol.

No.	Reaction	A_0	b_0	E_0
5.	$H + O_2\ (+\ M) \Leftrightarrow HO_2\ (+\ M)$	$5.2669 \cdot 10^{19}$	−1.3737	0
14.	$2OH\ (+\ M) \Leftrightarrow H_2O_2\ (+\ M)$	$1.9928 \cdot 10^{18}$	−1.178	$-5.2382 \cdot 10^3$
22.	$O_3\ (+\ M) \Leftrightarrow O + O_2\ (+\ M)$	$2.275 \cdot 10^{28}$	−4.37	$2.7297 \cdot 10^4$

Table A.10
The Troe-parameters of the pressure-dependent reactions.

No.	Reaction	$\alpha\,[-]$	T^{***} [K]	T^{*} [K]	T^{**} [K]
5.	$H + O_2\ (+\ M) \Leftrightarrow HO_2\ (+\ M)$	0.67	10^{-30}	10^{30}	10^{30}
14.	$2OH\ (+\ M) \Leftrightarrow H_2O_2\ (+\ M)$	0.43	10^{-30}	10^{30}	10^{30}
22.	$O_3\ (+\ M) \Leftrightarrow O + O_2\ (+\ M)$	0.6417	$3.91 \cdot 10^{-4}$	$8.6807 \cdot 10^3$	$6.0607 \cdot 10^3$

Appendix B. Arrhenius-constants of the three other models

It is worth to mention that these three models calculate the backward rate coefficients k_b from separate Arrhenius constants, similarly to the forward rate coefficients. These constants are indicated with subscript b. Where specific third-body coefficients are used, they are shown under the reaction line (Tables B.11–B.13).

Table B11
Arrhenius-coefficients for the model KAMATH1993. Subscripts *f* and *b* refer to backward and forward directions, respectively. The units for A_f and A_b are in 1/s for first order reactions, and in cm^3/mol·s for second order reactions. The units for E_f and E_b are in cal/mol. The enhanced third-body efficiencies are indicated at the specific reactions.

No.	Reaction	A_f	b_f	E_f	A_b	b_b	E_b
1.	$H + OH + M \Leftrightarrow H_2O + M$ H_2: 2.5 H_2O: 16	$2.25{\cdot}10^{22}$	−2	0	$1.96{\cdot}10^{22}$	−1.62	$1.186{\cdot}10^{5}$
2.	$2O + M \Leftrightarrow O_2 + M$ H_2: 2.5 H_2O: 16	$6.17{\cdot}10^{15}$	−0.5	0	$1.58{\cdot}10^{17}$	−0.5	$1.1818{\cdot}10^{5}$
3.	$O + H + M \Leftrightarrow OH + M$ H_2O: 5	$4.72{\cdot}10^{18}$	−1	0	$4.66{\cdot}10^{17}$	−0.65	$1.0166{\cdot}10^{5}$
4.	$H + O_2 \Leftrightarrow O + OH$	$1.92{\cdot}10^{14}$	0	$1.644{\cdot}10^{4}$	$7.18{\cdot}10^{11}$	0.36	$-6.79{\cdot}10^{2}$
5.	$H + O_2 + M \Leftrightarrow HO_2 + M$ H_2: 2.5 H_2O: 16	$2{\cdot}10^{15}$	0	$-1{\cdot}10^{3}$	$2.46{\cdot}10^{15}$	0	$4.829{\cdot}10^{4}$
6.	$2OH \Leftrightarrow O + H_2O$	$2.1{\cdot}10^{8}$	1.4	$3.97{\cdot}10^{2}$	$2.21{\cdot}10^{9}$	1.4	$1.6628{\cdot}10^{4}$
7.	$H + HO_2 \Leftrightarrow H_2 + O_2$	$6.63{\cdot}10^{13}$	0	$2.126{\cdot}10^{3}$	$2.19{\cdot}10^{13}$	0.28	$5.642{\cdot}10^{4}$
8.	$H + HO_2 \Leftrightarrow 2OH$	$1.69{\cdot}10^{14}$	0	$8.74{\cdot}10^{2}$	$1.08{\cdot}10^{11}$	0.61	$3.622{\cdot}10^{4}$
9.	$O + HO_2 \Leftrightarrow OH + O_2$	$1.81{\cdot}10^{13}$	0	$-4{\cdot}10^{2}$	$3.1{\cdot}10^{12}$	0.26	$5.1832{\cdot}10^{4}$
10.	$OH + HO_2 \Leftrightarrow O_2 + H_2O$	$1.45{\cdot}10^{16}$	−1	0	$2.18{\cdot}10^{16}$	−0.72	$6.9181{\cdot}10^{4}$
11.	$2H + M \Leftrightarrow H_2 + M$ H_2: 2.5 H_2O: 16	$2.45{\cdot}10^{20}$	−1.78	$9.6{\cdot}10^{2}$	$4.58{\cdot}10^{19}$	−1.4	$1.044{\cdot}10^{5}$
12.	$O + H_2 \Leftrightarrow H + OH$	$5.08{\cdot}10^{4}$	2.67	$6.292{\cdot}10^{3}$	$2.64{\cdot}10^{4}$	2.65	$4.462{\cdot}10^{3}$
13.	$H_2 + OH \Leftrightarrow H + H_2O$	$2.18{\cdot}10^{8}$	1.51	$3.43{\cdot}10^{3}$	$1.02{\cdot}10^{9}$	1.51	$1.862{\cdot}10^{4}$
14.	$2OH + M \Leftrightarrow H_2O_2 + M$ H_2: 2.5 H_2O: 16	$9{\cdot}10^{11}$	0.9	$-6.062{\cdot}10^{3}$	$1.2{\cdot}10^{17}$	0	$4.55{\cdot}10^{4}$
15.	$H + H_2O_2 \Leftrightarrow OH + H_2O$	$3.2{\cdot}10^{14}$	0	$8.96{\cdot}10^{3}$	$1.14{\cdot}10^{9}$	1.36	$7.587{\cdot}10^{4}$
16.	$H + H_2O_2 \Leftrightarrow H_2 + HO_2$	$4.82{\cdot}10^{13}$	0	$7.948{\cdot}10^{3}$	$1.41{\cdot}10^{11}$	0.66	$2.448{\cdot}10^{4}$
17.	$O + H_2O_2 \Leftrightarrow OH + HO_2$	$9.55{\cdot}10^{6}$	2	$3.97{\cdot}10^{3}$	$4.62{\cdot}10^{3}$	2.75	$1.8435{\cdot}10^{4}$
18.	$OH + H_2O_2 \Leftrightarrow H_2O + HO_2$	$1{\cdot}10^{13}$	0	$1.8{\cdot}10^{3}$	$2.8{\cdot}10^{13}$	0	$3.279{\cdot}10^{4}$
19.	$2HO_2 \Leftrightarrow O_2 + H_2O_2$	$3{\cdot}10^{12}$	0	$1.387{\cdot}10^{3}$	$4.53{\cdot}10^{14}$	−0.39	$3.914{\cdot}10^{4}$

Table B12
Arrhenius-coefficients for the model YASUI2003. Subscripts *f* and *b* refer to backward and forward directions, respectively. The units for A_f and A_b are in 1/s for first order reactions, and in cm^3/mol·s for second order reactions. The units for E_f and E_b are in cal/mol. The enhanced third-body efficiencies are indicated at the specific reactions.

No.	Reaction	A_f	b_f	E_f	A_b	b_b	E_b
1.	$H + OH + M \Leftrightarrow H_2O + M$ H_2: 2.5 H_2O: 16	$2.25{\cdot}10^{16}$	−2	0	$1.96{\cdot}10^{16}$	−1.62	$1.4543{\cdot}10^{5}$
2.	$2O + M \Leftrightarrow O_2 + M$ H_2: 2.5 H_2O: 16	$6.17{\cdot}10^{9}$	−0.5	0	$1.58{\cdot}10^{11}$	−0.5	$1.4487{\cdot}10^{5}$
3.	$O + H + M \Leftrightarrow OH +$ H_2O: 5	$4.72{\cdot}10^{12}$	−1	0	$4.66{\cdot}10^{11}$	−0.65	$1.2472{\cdot}10^{5}$
4.	$H + O_2 \Leftrightarrow O + OH$	$1.92{\cdot}10^{14}$	0	$2.0146{\cdot}10^{4}$	$7.18{\cdot}10^{11}$	0.36	$-8.3311{\cdot}10^{2}$
5.	$H + O_2 + M \Leftrightarrow HO_2 + M$ H_2: 2.5 H_2O: 16	$2{\cdot}10^{9}$	0	$-1.218{\cdot}10^{3}$	$2.46{\cdot}10^{9}$	0	$5.9195{\cdot}10^{4}$
6.	$2OH \Leftrightarrow O + H_2O$	$2.1{\cdot}10^{8}$	1.4	$4.872{\cdot}10^{2}$	$2.21{\cdot}10^{9}$	1.4	$2.0384{\cdot}10^{4}$
7.	$H + HO_2 \Leftrightarrow H_2 + O_2$	$6.63{\cdot}10^{13}$	0	$2.6065{\cdot}10^{3}$	$2.19{\cdot}10^{13}$	0.28	$6.9158{\cdot}10^{4}$
8.	$H + HO_2 \Leftrightarrow 2OH$	$1.69{\cdot}10^{14}$	0	$1.0718{\cdot}10^{3}$	$1.08{\cdot}10^{11}$	0.61	$4.4408{\cdot}10^{4}$
9.	$O + HO_2 \Leftrightarrow OH + O_2$	$1.81{\cdot}10^{13}$	0	$-4.872{\cdot}10^{2}$	$3.1{\cdot}10^{12}$	0.26	$6.3538{\cdot}10^{4}$
10.	$OH + HO_2 \Leftrightarrow O_2 + H_2O$	$1.45{\cdot}10^{16}$	−1	0	$2.18{\cdot}10^{16}$	−0.72	$8.4805{\cdot}10^{4}$
11.	$2H + M \Leftrightarrow H_2 + M$ H_2: 2.5 H_2O: 16	$2.45{\cdot}10^{14}$	−1.78	$1.1693{\cdot}10^{3}$	$4.58{\cdot}10^{13}$	−1.4	$1.2789{\cdot}10^{5}$
12.	$O + H_2 \Leftrightarrow H + OH$	$5.08{\cdot}10^{4}$	2.67	$7.7124{\cdot}10^{3}$	$2.64{\cdot}10^{4}$	2.65	$5.4688{\cdot}10^{3}$
13.	$H_2 + OH \Leftrightarrow H + H_2O$	$2.18{\cdot}10^{8}$	1.51	$4.2045{\cdot}10^{3}$	$1.02{\cdot}10^{9}$	1.51	$2.2825{\cdot}10^{4}$
14.	$2OH + M \Leftrightarrow H_2O_2 + M$ H_2: 2.5 H_2O: 16	$9{\cdot}10^{5}$	0.9	$-7.4298{\cdot}10^{3}$	$1.2{\cdot}10^{11}$	0	$5.5784{\cdot}10^{4}$
15.	$H + H_2O_2 \Leftrightarrow OH + H_2O$	$3.2{\cdot}10^{14}$	0	$1.0986{\cdot}10^{4}$	$1.14{\cdot}10^{9}$	1.36	$9.3007{\cdot}10^{4}$
16.	$H + H_2O_2 \Leftrightarrow H_2 + HO_2$	$4.82{\cdot}10^{13}$	0	$9.744{\cdot}10^{3}$	$1.41{\cdot}10^{11}$	0.66	$3.0012{\cdot}10^{4}$
17.	$O + H_2O_2 \Leftrightarrow OH + HO_2$	$9.55{\cdot}10^{6}$	2	$4.872{\cdot}10^{3}$	$4.62{\cdot}10^{3}$	2.75	$2.2599{\cdot}10^{4}$
18.	$OH + H_2O_2 \Leftrightarrow H_2O + HO_2$	$1{\cdot}10^{13}$	0	$2.1924{\cdot}10^{3}$	$2.8{\cdot}10^{13}$	0	$4.0194{\cdot}10^{4}$
19.	$2HO_2 \Leftrightarrow O_2 + H_2O_2$	$3{\cdot}10^{12}$	0	$1.7052{\cdot}10^{3}$	$4.53{\cdot}10^{14}$	−0.39	$4.7989{\cdot}10^{4}$
20.	$O_3 + M \Leftrightarrow O + O_2 + M$ O_2: 1.63 H_2O: 15	$2.48{\cdot}10^{8}$	0	$2.7844{\cdot}10^{4}$	$4.1{\cdot}10^{6}$	0	$-2.5749{\cdot}10^{3}$
21.	$H + O_3 \Leftrightarrow OH + O_2$	$2.3{\cdot}10^{11}$	0.75	0	$4.4{\cdot}10^{7}$	1.44	$9.403{\cdot}10^{4}$
22.	$H + O_3 \Leftrightarrow O + HO_2$	$9{\cdot}10^{12}$	0.5	$4.8964{\cdot}10^{3}$	0	0	0
23.	$OH + O_3 \Leftrightarrow O_2 + HO_2$	$7.8{\cdot}10^{11}$	0	$2.3386{\cdot}10^{3}$	0	0	0
24.	$HO_2 + O_3 \Leftrightarrow OH + 2O_2$	$1{\cdot}10^{11}$	0	$3.4348{\cdot}10^{3}$	0	0	0
25.	$O + O_3 \Leftrightarrow 2O_2$	$5.2{\cdot}10^{12}$	0	$5.0912{\cdot}10^{3}$	$1.2{\cdot}10^{13}$	0	$1.2131{\cdot}10^{5}$

Table B13
Arrhenius-coefficients for the model Merouani2014. Subscripts *f* and *b* refer to backward and forward directions, respectively. The units for A_f and A_b are in 1/s for first order reactions, and in cm^3/mol·s for second order reactions. The units for E_f and E_b are in cal/mol. The third-body coefficients are not indicated in the article [67], thus it was supposed to be 1 for all components.

No.	Reaction	A_f	b_f	E_f	A_b	b_b	E_b
1.	$H + OH + M \Leftrightarrow H_2O + M$	$2.2{\cdot}10^{22}$	−2	0	$1.912{\cdot}10^{23}$	−1.83	$1.185{\cdot}10^{5}$
2.	$2O + M \Leftrightarrow O_2 + M$	$6.165{\cdot}10^{15}$	−0.5	0	$4.515{\cdot}10^{17}$	−0.64	$1.189{\cdot}10^{5}$
3.	$O + H + M \Leftrightarrow OH + M$	$4.714{\cdot}10^{18}$	−1	0	$9.88{\cdot}10^{17}$	−0.74	$1.021{\cdot}10^{5}$
4.	$H + O_2 \Leftrightarrow O + OH$	$1.915{\cdot}10^{14}$	0	$1.644{\cdot}10^{4}$	$5.481{\cdot}10^{11}$	0.39	$-2.93{\cdot}10^{2}$
5.	$H + O_2 + M \Leftrightarrow HO_2 + M$	$1.475{\cdot}10^{12}$	0.6	0	$3.09{\cdot}10^{12}$	0.53	$4.887{\cdot}10^{4}$
6.	$2OH \Leftrightarrow O + H_2O$	$1.465{\cdot}10^{5}$	2.11	$-2.904{\cdot}10^{3}$	$2.97{\cdot}10^{6}$	2.02	$1.34{\cdot}10^{4}$
7.	$H + HO_2 \Leftrightarrow H_2 + O_2$	$1.66{\cdot}10^{13}$	0	$8.23{\cdot}10^{2}$	$3.164{\cdot}10^{12}$	0.35	$5.551{\cdot}10^{4}$
8.	$H + HO_2 \Leftrightarrow 2OH$	$7.079{\cdot}10^{13}$	0	$2.95{\cdot}10^{2}$	$2.027{\cdot}10^{10}$	0.72	$3.684{\cdot}10^{4}$
9.	$O + HO_2 \Leftrightarrow OH + O_2$	$3.25{\cdot}10^{13}$	0	0	$3.252{\cdot}10^{12}$	0.33	$5.328{\cdot}10^{4}$
10.	$OH + HO_2 \Leftrightarrow O_2 + H_2O$	$2.89{\cdot}10^{13}$	0	$-4.97{\cdot}10^{2}$	$5.861{\cdot}10^{13}$	0.24	$6.908{\cdot}10^{4}$
11.	$2H + M \Leftrightarrow H_2 + M$	$1.146{\cdot}10^{20}$	−1.68	$8.2{\cdot}10^{2}$	$4.577{\cdot}10^{19}$	−1.4	$1.044{\cdot}10^{5}$
12.	$O + H_2 \Leftrightarrow H + OH$	$3.82{\cdot}10^{12}$	0	$7.948{\cdot}10^{3}$	$2.667{\cdot}10^{4}$	2.65	$4.88{\cdot}10^{3}$
13.	$H_2 + OH \Leftrightarrow H + H_2O$	$2.16{\cdot}10^{8}$	1.52	$3.45{\cdot}10^{3}$	$2.298{\cdot}10^{9}$	1.4	$1.832{\cdot}10^{4}$
14.	$2OH + M \Leftrightarrow H_2O_2 + M$	$1{\cdot}10^{14}$	−0.37	0	$2.951{\cdot}10^{14}$	0	$4.843{\cdot}10^{4}$
15.	$H + H_2O_2 \Leftrightarrow OH + H_2O$	$2.41{\cdot}10^{13}$	0	$3.97{\cdot}10^{3}$	$1.269{\cdot}10^{8}$	1.31	$7.141{\cdot}10^{4}$
16.	$H + H_2O_2 \Leftrightarrow H_2 + HO_2$	$6.025{\cdot}10^{13}$	0	$7.95{\cdot}10^{3}$	$1.041{\cdot}10^{11}$	0.7	$2.395{\cdot}10^{4}$
17.	$O + H_2O_2 \Leftrightarrow OH + HO_2$	$9.55{\cdot}10^{6}$	2	$3.97{\cdot}10^{3}$	$8.66{\cdot}10^{3}$	2.68	$1.856{\cdot}10^{4}$
18.	$OH + H_2O_2 \Leftrightarrow H_2O + HO_2$	$1{\cdot}10^{12}$	0	0	$1.838{\cdot}10^{10}$	0.59	$3.089{\cdot}10^{4}$
19.	$2HO_2 \Leftrightarrow O_2 + H_2O_2$	$4.2{\cdot}10^{14}$	0	$1.198{\cdot}10^{4}$	$4.643{\cdot}10^{16}$	−0.35	$5.067{\cdot}10^{4}$

Appendix C. Supplementary data

The supplementary material includes figures of the yields for all the chemical substances as a function of the pressure amplitude similarly to Figs. 5–8. The employed MATLAB code is also included for reproducibility reasons (made in version R2020a). Finally, the CHEMKIN input files for the four chemical mechanisms are attached, as well. Supplementary data associated with this article can be found, in the online version, at https://doi.org/10.1016/j.ultsonch.2022.105925.

References

[1] T.G. Leighton, The acoustic bubble, Academic Press, London, 2012.
[2] R. Mettin, From a single bubble to bubble structures in acoustic cavitation, in: Oscillations, Waves and Interactions: Sixty Years Drittes Physikalisches Institut; a Festschrift, Universitätsverlag Göttingen, Göttingen, Germany, 2007.
[3] J. Rosselló, W. Lauterborn, M. Koch, T. Wilken, T. Kurz, R. Mettin, Acoustically induced bubble jets, Phys. Fluids 30 (12) (2018), 122004.
[4] R. Mettin, Bubble structures in acoustic cavitation, in: Bubble and Particle Dynamics in Acoustic Fields: Modern Trends and Applications, Research Signpost, Trivandrum, Kerala, India, 2005.
[5] H. Haghi, A. Sojahrood, M.C. Kolios, Collective nonlinear behavior of interacting polydisperse microbubble clusters, Ultrason. Sonochem. 58 (2019), 104708.
[6] P.M. Kanthale, A. Brotchie, M. Ashokkumar, F. Grieser, Experimental and theoretical investigations on sonoluminescence under dual frequency conditions, Ultrason. Sonochem. 15 (4) (2008) 629–635.
[7] R. Urteaga, D. Dellavale, G.F. Puente, F.J. Bonetto, Experimental study of transient paths to the extinction in sonoluminescence, J. Acoust. Soc. Am. 124 (3) (2008) 1490–1496.
[8] M. Koch, J.M. Rosselló, C. Lechner, W. Lauterborn, J. Eisener, R. Mettin, Theory-assisted optical ray tracing to extract cavitation-bubble shapes from experiment, Exp. Fluids 62 (3) (2021) 1–19.
[9] Y. Zhang, F. Chen, Y. Zhang, X. Du, Experimental investigations of interactions between a laser-induced cavitation bubble and a spherical particle, Exp. Thermal Fluid Sci. 98 (2018) 645–661.
[10] A. Sojahrood, R. Earl, H. Haghi, Q. Li, T. Porter, M. Kolios, R. Karshafian, Nonlinear dynamics of acoustic bubbles excited by their pressure-dependent subharmonic resonance frequency: influence of the pressure amplitude, frequency, encapsulation and multiple bubble interactions on oversaturation and enhancement of the subharmonic signal, Nonlinear Dyn. 103 (1) (2021) 429–466.
[11] D. Schanz, B. Metten, T. Kurz, W. Lauterborn, Molecular dynamics simulations of cavitation bubble collapse and sonoluminescence, New J. Phys. 14 (11) (2012), 113019.
[12] K. Young Kim, K.-T. Byun, H.-Y. Kwak, Characteristics of sonoluminescing bubbles in aqueous solutions of sulfuric acid, J. Phys. Soc. Jpn. 75 (11) (2006), 114705.
[13] K.S. Suslick, N.C. Eddingsaas, D.J. Flannigan, S.D. Hopkins, H. Xu, The chemical history of a bubble, Accounts Chem. Res. 51 (9) (2018) 2169–2178.
[14] P. Kanthale, M. Ashokkumar, F. Grieser, Sonoluminescence, sonochemistry (H_2O_2 yield) and bubble dynamics: frequency and power effects, Ultrason. Sonochem. 15 (2) (2008) 143–150.
[15] J. Rooze, E.V. Rebrov, J.C. Schouten, J.T. Keurentjes, Dissolved gas and ultrasonic cavitation–a review, Ultrason. Sonochem. 20 (1) (2013) 1–11.
[16] C. Pétrier, A. Francony, Ultrasonic waste-water treatment: incidence of ultrasonic frequency on the rate of phenol and carbon tetrachloride degradation, Ultrason. Sonochem. 4 (4) (1997) 295–300.
[17] V.L. Gole, A. Fishgold, R. Sierra-Alvarez, P. Deymier, M. Keswani, Treatment of perfluorooctane sulfonic acid (PFOS) using a large-scale sonochemical reactor, Sep. Purif. Technol. 194 (2018) 104–110.
[18] M. Draye, N. Kardos, Advances in green organic sonochemistry, Top. Curr. Chem. (Z) 374 (74) (2016) 1–29.
[19] F. Dang, K. Kato, H. Imai, S. Wada, H. Haneda, M. Kuwabara, Characteristics of batio3 particles sonochemically synthesized in aqueous solution, Jpn. J. Appl. Phys. 48 (9S1) (2009) 09KC02.
[20] K. Yasui, K. Kato, Numerical simulations of sonochemical production and oriented aggregation of $BaTiO_3$ nanocrystals, Ultrason. Sonochem. 35 (2017) 673–680.
[21] T.J. Mason, Ultrasound in synthetic organic chemistry, Chem. Soc. Rev. 26 (6) (1997) 443–451.
[22] S.V. Sancheti, P.R. Gogate, A review of engineering aspects of intensification of chemical synthesis using ultrasound, Ultrason. Sonochem. 36 (2017) 527–543.
[23] V. Mišík, P. Riesz, Free radical intermediates in sonodynamic therapy, Ann. N. Y. Acad. Sci. 899 (1) (2000) 335–348.
[24] I. Rosenthal, J.Z. Sostaric, P. Riesz, Sonodynamic therapy—-a review of the synergistic effects of drugs and ultrasound, Ultrason. Sonochem. 11 (6) (2004) 349–363.
[25] K. Tachibana, L.B. Feril Jr, Y. Ikeda-Dantsuji, Sonodynamic therapy, Ultrasonics 48 (4) (2008) 253–259.
[26] A.J. Sojahrood, Q. Li, H. Haghi, R. Karshafian, T.M. Porter, M.C. Kolios, Towards the accurate characterization of the shell parameters of microbubbles based on attenuation and sound speed measurements, J. Acoust. Soc. Am. 141 (5) (2017) 3493.
[27] K. Klapcsik, R. Varga, F. Hegedűs, Bi-parametric topology of subharmonics of an asymmetric bubble oscillator at high dissipation rate, Nonlinear Dyn. 94 (4) (2018) 2373–2389.
[28] A. Sojahrood, H. Haghi, R. Karshafian, M.C. Kolios, Classification of the major nonlinear regimes of oscillations, oscillation properties, and mechanisms of wave energy dissipation in the nonlinear oscillations of coated and uncoated bubbles, Phys. Fluids 33 (1) (2021), 016105.
[29] G. Hauke, D. Fuster, C. Dopazo, Dynamics of a single cavitating and reacting bubble, Phys. Rev. E 75 (6) (2007), 066310.
[30] F. Cavalieri, F. Chemat, K. Okitsu, A. Sambandam, K. Yasui, B. Zisu, Handbook of Ultrasonics and Sonochemistry, 1st Edition, Springer Singapore, Singapore, 2016.

[31] A.J. Sojahrood, D. Wegierak, H. Haghi, R. Karshfian, M.C. Kolios, A simple method to analyze the super-harmonic and ultra-harmonic behavior of the acoustically excited bubble oscillator, Ultrason. Sonochem. 54 (2019) 99–109.
[32] M. Wang, Y. Zhou, Numerical investigation of the inertial cavitation threshold by dual-frequency excitation in the fluid and tissue, Ultrason. Sonochem. 42 (2018) 327–338.
[33] F. Hegedűs, K. Klapcsik, W. Lauterborn, U. Parlitz, R. Mettin, GPU accelerated study of a dual-frequency driven single bubble in a 6-dimensional parameter space: The active cavitation threshold, Ultrason. Sonochem. 67 (2020), 105067.
[34] K. Klapcsik, GPU accelerated numerical investigation of the spherical stability of an acoustic cavitation bubble excited by dual-frequency, Ultrason. Sonochem. 77 (2021), 105684.
[35] P.A. Tatake, A.B. Pandit, Modelling and experimental investigation into cavity dynamics and cavitational yield: influence of dual frequency ultrasound sources, Chem. Eng. Sci. 57 (22–23) (2002) 4987–4995.
[36] M. Guédra, C. Inserra, B. Gilles, Accompanying the frequency shift of the nonlinear resonance of a gas bubble using a dual-frequency excitation, Ultrason. Sonochem. 38 (2017) 298–305.
[37] H.G. Flynn, Cavitation dynamics. i. a mathematical formulation, J. Acoust. Soc. Am. 57 (6) (1975) 1379–1396.
[38] H. Flynn, C.C. Church, A mechanism for the generation of cavitation maxima by pulsed ultrasound, J. Acoust. Soc. Am. 76 (2) (1984) 505–512.
[39] C. Kalmár, K. Klapcsik, F. Hegedűs, Relationship between the radial dynamics and the chemical production of a harmonically driven spherical bubble, Ultrason. Sonochem. 64 (2020), 104989.
[40] S. Sochard, A.M. Wilhelm, H. Delmas, Modelling of free radicals production in a collapsing gas-vapour bubble, Ultrason. Sonochem. 4 (2) (1997) 77–84.
[41] A.J. Colussi, L.K. Weavers, M.R. Hoffmann, Chemical bubble dynamics and quantitative sonochemistry, J. Phys. Chem. A 102 (35) (1998) 6927–6934.
[42] O. Authier, H. Ouhabaz, S. Bedogni, Modeling of sonochemistry in water in the presence of dissolved carbon dioxide, Ultrason. Sonochem. 45 (2018) 17–28.
[43] X. Lu, A. Prosperetti, R. Toegel, D. Lohse, Harmonic enhancement of single-bubble sonoluminescence, Phys. Rev. E 67 (5) (2003), 056310.
[44] B.D. Storey, A.J. Szeri, Water vapour, sonoluminescence and sonochemistry, Proc. R. Soc. Lond. A 456 (1999) (2000) 1685–1709.
[45] K. Yasui, Effects of thermal conduction on bubble dynamics near the sonoluminescence threshold, J. Acoust. Soc. Am. 98 (5) (1995) 2772–2782.
[46] K. Yasui, Variation of liquid temperature at bubble wall near the sonoluminescence threshold, J. Phys. Soc. Jpn. 65 (9) (1996) 2830–2840.
[47] K. Yasui, Alternative model of single-bubble sonoluminescence, Phys. Rev. E 56 (6) (1997) 6750.
[48] K. Yasui, T. Tuziuti, Y. Iida, H. Mitome, Theoretical study of the ambient-pressure dependence of sonochemical reactions, J. Chem. Phys. 119 (1) (2003) 346–356.
[49] K. Yasui, T. Tuziuti, Y. Iida, Optimum bubble temperature for the sonochemical production of oxidants, Ultrason. Sonochem. 42 (1–9) (2004) 579–584.
[50] K. Yasui, T. Tuziuti, T. Kozuka, A. Towata, Y. Iida, Relationship between the bubble temperature and main oxidant created inside an air bubble under ultrasound, J. Chem. Phys. 127 (15) (2007), 154502.
[51] K. Yasui, T. Tuziuti, J. Lee, T. Kozuka, A. Towata, Y. Iida, The range of ambient radius for an active bubble in sonoluminescence and sonochemical reactions, J. Chem. Phys. 128 (18) (2008), 184705.
[52] V. Kamath, A. Prosperetti, F. Egolfopoulos, A theoretical study of sonoluminescence, J. Acoust. Soc. Am. 94 (1) (1993) 248–260.
[53] F. Egolfopoulos, C.K. Law, An experimental and computational study of the burning rates of ultra-lean to moderately-rich $H_2/O_2/N_2$ laminar flames with pressure variations, Proc. Combust. Inst. 23 (1991) 333–340.
[54] A. Prosperetti, The thermal behaviour of oscillating gas bubbles, J. Fluid Mech. 222 (1991) 587–616.
[55] R. Toegel, B. Gompf, R. Pecha, D. Lohse, Does water vapor prevent upscaling sonoluminescence? Phys. Rev. Lett. 85 (15) (2000) 3165.
[56] L. Stricker, A. Prosperetti, D. Lohse, Validation of an approximate model for the thermal behavior in acoustically driven bubbles, J. Acoust. Soc. Am. 130 (5) (2011) 3243–3251.
[57] R. Toegel, D. Lohse, Phase diagrams for sonoluminescing bubbles: A comparison between experiment and theory, J. Chem. Phys. 118 (4) (2003) 1863–1875.
[58] L. Stricker, D. Lohse, Radical production inside an acoustically driven microbubble, Ultrason. Sonochem. 21 (1) (2014) 336–345.
[59] S. Merouani, O. Hamdaoui, Y. Rezgui, M. Guemini, Computer simulation of chemical reactions occurring in collapsing acoustical bubble: dependence of free radicals production on operational conditions, Res. Chem. Intermediat. 41 (2) (2015) 881–897.
[60] S. Merouani, O. Hamdaoui, Y. Rezgui, M. Guemini, Mechanism of the sonochemical production of hydrogen, Int. J. Hydrogen Energy 40 (11) (2015) 4056–4064.
[61] K. Kerboua, O. Hamdaoui, Influence of reactions heats on variation of radius, temperature, pressure and chemical species amounts within a single acoustic cavitation bubble, Ultrason. Sonochem. 41 (2018) 449–457.
[62] S. Merouani, O. Hamdaoui, Y. Rezgui, M. Guemini, Sensitivity of free radicals production in acoustically driven bubble to the ultrasonic frequency and nature of dissolved gases, Ultrason. Sonochem. 22 (2015) 41–50.
[63] K. Kerboua, O. Hamdaoui, Numerical investigation of the effect of dual frequency sonication on stable bubble dynamics, Ultrason. Sonochem. 49 (2018) 325–332.
[64] K. Kerboua, O. Hamdaoui, A. Alghyamah, Energy balance of high-energy stable acoustic cavitation within dual-frequency sonochemical reactor, Ultrason. Sonochem. 73 (2021), 105471.
[65] W.C.J. Gardiner, Combustion Chemistry, Springer-Verlag, New York, 1984.
[66] D. Baulch, M. Bowers, D. Malcolm, R. Tuckerman, Evaluated kinetic data for high-temperature reactions, volume 5, part 1: Homogeneous gas phase reactions of the hydroxyl radical with alkanes, J. Phys. Chem. Ref. Data 15 (2) (1986) 465–592.
[67] S. Merouani, O. Hamdaoui, Y. Rezgui, M. Guemini, Theoretical estimation of the temperature and pressure within collapsing acoustical bubbles, Ultrason. Sonochem. 21 (1) (2014) 53–59.
[68] NIST Chemical Kinetics Database (2022). URL: https://kinetics.nist.gov/kinetics/.
[69] k-evaluation web page (2022). URL: https://k-evaluation.elte.hu/.
[70] W. Lauterborn, T. Kurz, Physics of bubble oscillations, Rep. Prog. Phys. 73 (10) (2010), 106501.
[71] A. Prosperetti, A. Lezzi, Bubble dynamics in a compressible liquid. Part 1. First-order theory, J. Fluid Mech. 168 (1986) 457–478.
[72] S. Gordon, Computer program for calculation of complex chemical equilibrium compositions, rocket performance, incident and reflected shocks, and Chapman-Jouguet detonations, vol. 273, Scientific and Technical Information Office, National Aeronautics and Space Administration, 1976.
[73] A.V. Pandit, V.P. Sarvothaman, V.V. Ranade, Estimation of chemical and physical effects of cavitation by analysis of cavitating single bubble dynamics, Ultrason. Sonochem. 77 (2021), 105677.
[74] G. Zhou, A. Prosperetti, Modelling the thermal behaviour of gas bubbles, Journal of Fluid Mechanics 901.
[75] S. Fujikawa, T. Akamatsu, Effects of the non-equilibrium condensation of vapour on the pressure wave produced by the collapse of a bubble in a liquid, J. Fluid Mech. 97 (3) (1980) 481–512.
[76] T. Turányi, A.S. Tomlin, Analysis of kinetic reaction mechanisms, Springer, 2014.
[77] T. Varga, C. Olm, T. Nagy, I.G. Zsély, É. Valkó, R. Pálvölgyi, H.J. Curran, T. Turányi, Development of a joint hydrogen and syngas combustion mechanism based on an optimization approach, Int. J. Chem. Kinet. 48 (8) (2016) 407–422.
[78] H. Zhao, X. Yang, Y. Ju, Kinetic studies of ozone assisted low temperature oxidation of dimethyl ether in a flow reactor using molecular-beam mass spectrometry, Combust. Flame 173 (2016) 187–194.
[79] T. Varga, T. Nagy, C. Olm, I.G. Zsély, R. Pálvölgyi, É. Valkó, G. Vincze, M. Cserháti, H.J. Curran, T. Turányi, Optimization of a hydrogen combustion mechanism using both direct and indirect measurements, Proc. Combust. Inst. 35 (1) (2015) 589–596.
[80] C. Olm, I.G. Zsély, T. Varga, H.J. Curran, T. Turányi, Comparison of the performance of several recent syngas combustion mechanisms, Combust. Flame 162 (5) (2015) 1793–1812.
[81] F.A. Lindemann, S. Arrhenius, I. Langmuir, N. Dhar, J. Perrin, W.M. Lewis, Discussion on "the radiation theory of chemical action", Trans. Faraday Soc. 17 (1922) 598–606.
[82] R. Gilbert, K. Luther, J. Troe, Theory of thermal unimolecular reactions in the fall-off range. II. weak collision rate constants, Berichte der Bunsengesellschaft für physikalische, Chemie 87 (2) (1983) 169–177.
[83] M.J. Pilling, P.W. Seakins, Reaction kinetics, Oxford University Press, 1995.
[84] K.A. Holbrook, M.J. Pilling, S.H. Robertson, Unimolecular reactions, second ed., John Wiley, New York, 1996.
[85] P. Atkins, J. De Paula, Atkins' Physical Chemistry, OUP Oxford, 2014.
[86] R. Toegel, S. Hilgenfeldt, D. Lohse, Suppressing dissociation in sonoluminescing bubbles: The effect of excluded volume, Phys. Rev. Lett. 88 (3) (2002), 034301.
[87] S.S. Rashwan, I. Dincer, A. Mohany, An investigation of ultrasonic based hydrogen production, Energy 205 (2020), 118006.
[88] K. Kerboua, S. Merouani, O. Hamdaoui, A. Alghyamah, M.H. Islam, H.E. Hansen, B. G. Pollet, How do dissolved gases affect the sonochemical process of hydrogen production? An overview of thermodynamic and mechanistic effects–on the "hot spot theory", Ultrason. Sonochem. 105422 (2020).
[89] M.H. Islam, J.J. Lamb, K.M. Lien, O.S. Burheim, J.-Y. Hihn, B.G. Pollet, Novel fuel production based on sonochemistry and sonoelectrochemistry, ECS Trans. 92 (10) (2019) 1.
[90] I. Iordache, M. Nechita, N. Aelenei, I. Rosca, G. Apostolescu, M. Peptanariu, Sonochemical enhancement of cyanide ion degradation from wastewater in the presence of hydrogen peroxide, Polish J. Environ. Stud. 12 (6) (2003) 735–738.
[91] M. Sivakumar, A. Gedanken, A sonochemical method for the synthesis of polyaniline and au–polyaniline composites using H_2O_2 for enhancing rate and yield, Synth. Met. 148 (3) (2005) 301–306.